CANCER

H3K9 dimethylation safeguards cancer cells against activation of the interferon pathway

Anne Meldgaard Hansen[1,2,3], Ying Ge[1,2,3], Mikkel Bruhn Schuster[1,2,3], Sachin Pundhir[1,2,3], Janus Schou Jakobsen[1,2,3], Adrija Kalvisa[1,2,3], Marta Cecylia Tapia[1,2,3], Sandra Gordon[2,3], Francesca Ambri[2,3], Frederik Otzen Bagger[1,2,3,4], Deo Pandey[2,5], Kristian Helin[2,3,6,7], Bo Torben Porse[1,2,3]*

Activation of interferon genes constitutes an important anticancer pathway able to restrict proliferation of cancer cells. Here, we demonstrate that the H3K9me3 histone methyltransferase (HMT) suppressor of variegation 3–9 homolog 1 (SUV39H1) is required for the proliferation of acute myeloid leukemia (AML) and find that its loss leads to activation of the interferon pathway. Mechanistically, we show that this occurs via destabilization of a complex composed of SUV39H1 and the two H3K9me2 HMTs, G9A and GLP. Indeed, loss of H3K9me2 correlated with the activation of key interferon pathway genes, and interference with the activities of G9A/GLP largely phenocopied loss of SUV39H1. Last, we demonstrate that inhibition of G9A/GLP synergized with DNA demethylating agents and that SUV39H1 constitutes a potential biomarker for the response to hypomethylation treatment. Collectively, we uncovered a clinically relevant role for H3K9me2 in safeguarding cancer cells against activation of the interferon pathway.

INTRODUCTION

Acute myeloid leukemia (AML) is the common term for a diverse group of highly aggressive hematopoietic malignancies characterized by the rapid accumulation of myeloid blasts in the bone marrow and sometimes in nonhematopoietic tissues. Standard treatment has only changed slightly over the past three to four decades, and the overall survival rates for AML patients remain below 50% (*1*). Hence, there is a strong need for the identification of previously unidentified targets for therapeutic intervention. AML arises as a result of genetic aberrations, which confer a proliferative and/or survival advantage on myeloid progenitor cells and/or impair their differentiation. In addition to genetic lesions, cancer cells may also exhibit aberrant epigenetic regulation or develop the so-called "oncogenic dependencies" of proteins, which are not crucial for cell survival in a normal physiological context (*2*, *3*). As neither of the latter two types of events necessarily depend on specific mutations, functional approaches are pivotal to study the heterogeneous changes, which are selected for during AML development and progression.

In eukaryotic cells, epigenetic regulation of gene expression is mainly achieved by DNA methylation and posttranslational modifications of the N-terminal tails of the core histones, resulting in different chromatin accessibility, depending on the position and type of modification. Factors editing or recognizing these modifications (referred to as epigenetic writers/erasers and readers, respectively) are among the most frequently mutated genes in leukemia as well as in other cancer types (*4*, *5*). Furthermore, several of these factors have been functionally validated as oncogenes or tumor suppressors. It is therefore widely accepted that epigenetic deregulation plays a major role in establishing and maintaining a malignant phenotype.

Suppressor of variegation 3–9 homolog 1 (SUV39H1) and its close homolog SUV39H2 are mammalian homologs of the *Drosophila* suppressor of variegation 3–9 [Su(var)3–9] and are both histone methyltransferases (HMTs), which, along with SETDB1, catalyze trimethylation of lysine 9 of histone H3 (H3K9) (*6*, *7*). This modification constitutes a repressive epigenetic mark, which is enriched in heterochromatin and functions as a binding site for repressive chromobox proteins such as Heterochromatin protein 1 (HP1) (*8*). SUV39H1 and SUV39H2 play highly overlapping physiological roles in maintaining heterochromatin stability. Studies in transgenic mice have demonstrated that, while a deficiency of either of the two factors does not result in any major phenotypes, the simultaneous ablation of both leads to male sterility, severely decreased survival, and sporadically occurring B cell lymphomas (*9*). At the mechanistic level, these phenotypes correlate with hypomethylation of H3K9 in the pericentric chromatin regions, aberrant chromosome segregation during meiosis and mitosis, as well as abnormally long telomeres (*9*, *10*).

While the physiological roles of SUV39H1 and SUV39H2 seem to be highly redundant, several studies have implicated specific roles of SUV39H1 as a tumor-promoting factor in various cancer types, including AML, and several distinct mechanisms have been proposed (*11*–*13*). First, tumor-specific gene expression has been suggested to occur via direct interactions between SUV39H1 and crucial players in leukemogenesis, such as the transcription factor Runt-related transcription factor 1, the fusion oncoprotein Promyelocytic leukemia protein - Retinoic acid receptor alpha (PML-RARa) and the oncogenic transcription factor Ecotropic Viral Integration Site 1 (EVI-1), thus facilitating the H3K9me3-mediated transcriptional repression of the cognate target genes (*11*–*15*). Furthermore, interaction with SUV39H1 has been demonstrated to be crucial for the potential of PML-RARA to block myeloid differentiation of U937 cells and for the potential of EVI-1 to immortalize primary bone marrow cells in vitro (*15*). Conversely, knockdown (KD) of *SUV39H1* can reinitiate expression of the tumor suppressor genes *CHD1* (E-cadherin) and

[1]The Finsen Laboratory, Rigshospitalet, Faculty of Health Sciences, University of Copenhagen, 2200 Copenhagen, Denmark. [2]Biotech Research and Innovation Center (BRIC), University of Copenhagen, 2200 Copenhagen, Denmark. [3]Novo Nordisk Foundation Center for Stem Cell Biology, DanStem, Faculty of Health Sciences, University of Copenhagen, 2200 Copenhagen, Denmark. [4]Center for Genomic Medicine, Copenhagen University Hospital, Copenhagen, Denmark. [5]Department of Microbiology, Oslo University Hospital, NO-0373 Oslo, Norway. [6]Cell Biology Program and Center for Epigenetics Research, Memorial Sloan Kettering Center, New York, NY 10065, USA. [7]The Institute of Cancer Research, London SW3 6JB, United Kingdom.
*Corresponding author. Email: bo.porse@finsenlab.dk

CDKN2B (p15INK4B) in three different AML cell lines (*16*). Last, SUV39H1 might also be influenced by (or influence) other epigenetic regulators. In particular, the fact that SUV39H1 and the two H3K9me2 HMTs, G9A and G9A-like protein (GLP), are found in a multiprotein complex is very intriguing (*17*).

While most of the mechanisms discussed above are centered on the context-dependent oncogenic functions of SUV39H1, the protein also has a more general role in regulating heterochromatin. Specifically, it is strongly connected to DNA methylation at heterochromatic regions and is involved in repressing retrotransposons. Recent data have indicated that treatment of various tumor cell lines with DNA methyltransferase inhibitors (DNMTis) leads to the expression of double-stranded RNA (dsRNA) from retrotransposons, which subsequently promotes an interferon (IFN) response, ultimately leading to growth inhibition (*18*, *19*). Conversely, SUV39H1 was shown to be required for the repression of RNA derived from long interspersed nuclear elements (LINEs) (*20*). This requirement was restricted to embryonic stem cells (ESCs), correlating with the hypomethylated state of ESC heterochromatin compared to more differentiated cell types. The finding that cancer cells are also, in general, associated with low levels of DNA methylation raises the possibility that SUV39H1 could be selectively important in these cells, compared to most somatic cell types to ensure the appropriate repression of the different types of retrotransposons (*21*, *22*).

Regardless of the mechanism(s) underlying its oncogenic potential, the potential of SUV39H1 as a novel druggable target is underscored by the capacity of the pan-SUV39H inhibitor, chaetocin, which targets both SUV39H1 and SUV39H2, to inhibit the growth of multiple myeloid cell lines and primary tumor material (*16*, *23*–*25*). Of particular interest are the observations that synergistic effects can be achieved between chaetocin and the chemotherapy agent, cytarabine, as well as with other drugs targeting epigenetic modulators with different substrates than H3K9 (*23*, *24*). One would expect selective inhibition of SUV39H1 to have very modest effects on normal cells because of the negligible phenotype following the complete loss of SUV39H1 activity. A further understanding of the mechanisms underlying the cancer-specific capacity of SUV39H1 to sustain cell growth would therefore be potentially beneficial for future treatment of AML and other cancer forms.

Thus, in the present work, we used a combination of murine in vivo models and human in vitro models to characterize the oncogenic capacity of SUV39H1 in AML, as well as the underlying mechanisms. Specifically, we find that the oncogenic effect of SUV39H1 is mainly facilitated via repression of IFN pathway genes and, unexpectedly, that this repression is orchestrated by stabilization of the HMTs G9A and GLP. Furthermore, we demonstrate a synergistic effect between the inhibition of the SUV39H1/G9A/GLP complex alongside derepression of retrotransposons with DNMTis, thereby providing a fertile ground for potential clinical translation.

RESULTS

SUV39H1 is a tumor-promoting factor in AML

To test the putative function of SUV39H1 as a tumor-promoting factor in vivo, we took advantage of a mouse model of *CEBPA* mutant AML. In this model, mice homozygous for an allele that solely expresses the leukemia-associated CEBPA-p30 isoform ($Cebpa^{Lp30/Lp30}$ from hereon Lp30) develop transplantable AML with a strong resemblance to human AML harboring the similar lesion (*26*, *27*). To test the impact of depleting SUV39H1 in the context of Lp30 AML, we performed a competitive transplantation assay. Briefly, Lp30 AML cells transduced with a retrovirus encoding an short hairpin RNA (shRNA)–targeting *Suv39h1* (green fluorescent protein, GFP^+) were transplanted into sublethally irradiated recipients in a 1:1 ratio with cells transduced with a retrovirus encoding a scrambled (Scr) shRNA [YFP^+ (yellow fluorescent protein positive)]. Arguing for its requirement for proliferation of AML, even a modest depletion of the *Suv39h1* transcript led to a massive reduction of the corresponding Lp30 AML cells in recipient mice (Fig. 1, A to C). When we performed a similar experiment in which the mixtures were generated from transduced cells harvested from primary recipients, *Suv39h1* KD cells were also out-competed, thereby ruling out the possibility that the effects were due to in vitro culturing before transplantation (Fig. 1D). Last, we assessed the impact of *Suv39h1* depletion on survival, by transplanting 10,000 sorted GFP^+ sh-Scr or sh-*Suv39h1*-expressing Lp30 cells, and found SUV39H1 depletion to significantly increase disease latency (Fig. 1E).

To test whether the functional impact of SUV39H1 could be extended to other AML models, we carried out survival analysis on recipients of murine AML cells transformed with retrovirally expressed MLL-AF9 fusion oncogene (*28*). Furthermore, to rule out the possibility that any observed phenotypes might be a consequence of shRNA off-target effects, we tested whether the phenotype could be rescued by overexpression of SUV39H1. To achieve this, we transduced MLL-AF9 AML cells with shRNA-expressing (*Suv39h1*-targeting or scrambled, YFP^+) and SUV39H1-expressing (or control; GFP^+) retroviruses and subsequently used sorted GFP/YFP double-positive cells for transplantation (fig. S1A). In the context of MLL-AF9–driven AML, *Suv39h1* KD resulted in longer latency times and in incomplete penetrance (fig. S1, B and C). This effect was rescued by overexpression of wild-type (WT) SUV39H1 but not by the catalytically dead SET domain mutant. We furthermore carried out an in vitro competitive proliferation experiment and demonstrated a mild competitive disadvantage of *Suv39h1* KD cells (fig. S1D). In concordance with the above-described limited phenotypes of full *Suv39h1* deficiency in vivo (*9*), normal $c\text{-}Kit^+$ stem and progenitor cells were unaffected by SUV39H1 depletion (fig. S1E).

Collectively, these findings extend previous in vitro observations by demonstrating the requirement of SUV39H1 in two distinct murine in vivo AML models. In agreement with the lack of phenotype observed in SUV39H1-deficient mice, we failed to detect an effect in normal hematopoietic cells.

SUV39H1 KD promotes growth arrest in human myeloid cells

Having established that SUV39H1 functions as an oncogene in two different murine AML models, and that the previously observed phenotypes in human myeloid cell lines are representative of an in vivo scenario, we next wanted to determine the mechanisms underlying this effect. To this end, we transduced the myeloid cell lines, THP-1, Kasumi-1, and U937, with lentiviral constructs encoding one of two *SUV39H1*-targeting shRNAs (or a scrambled control shRNA) and assessed the degree to which SUV39H1 depletion affected cell proliferation. Consistent with our murine data, we found that proliferation was severely impaired after *SUV39H1* KD in all three cell lines (Fig. 2A) and subsequently chose to put our main emphasis on the U937 cells, where assessment of mRNA and protein levels demonstrated KD efficiencies of about 80% (Fig. 2A and fig. S2A).

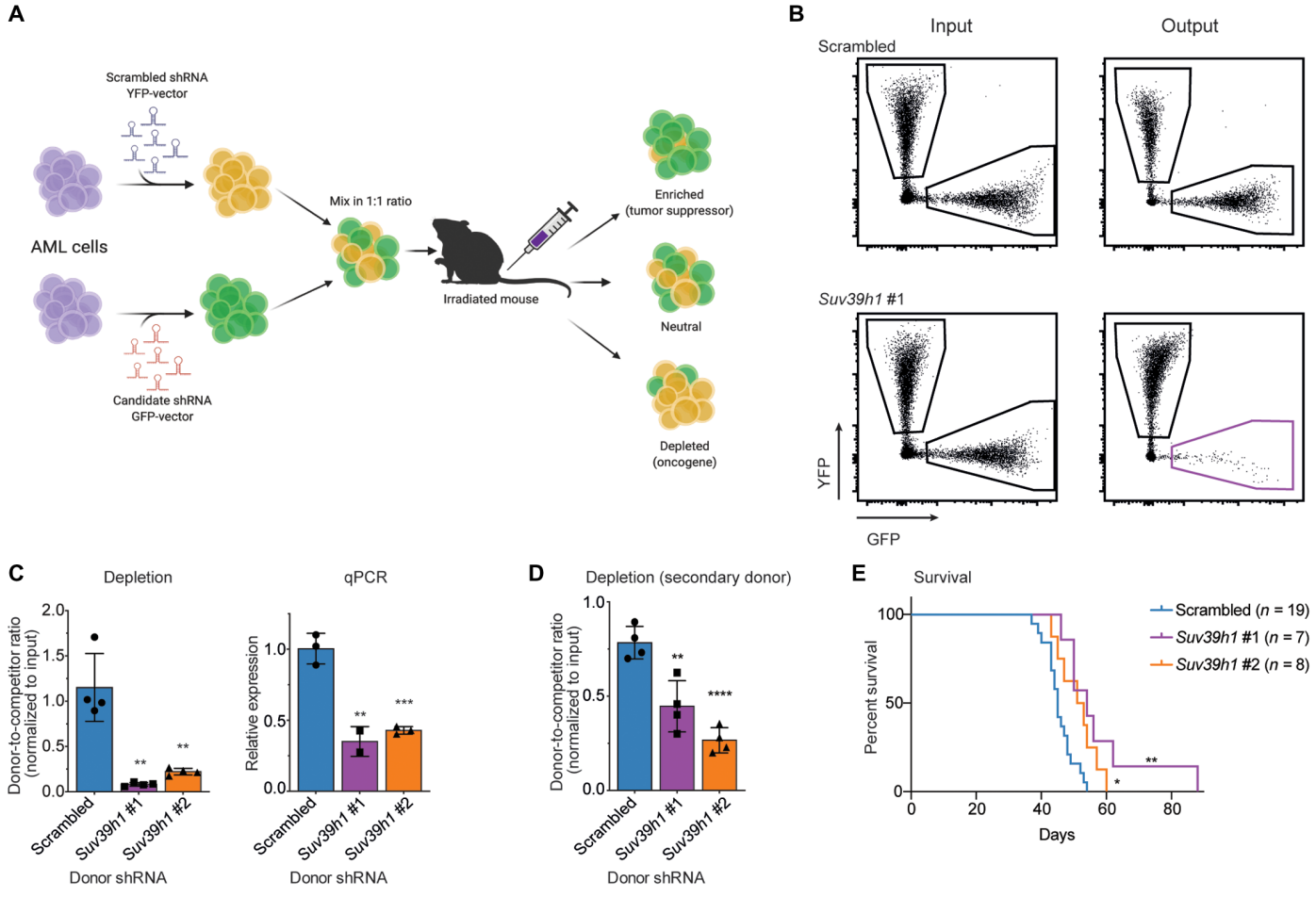

Fig. 1. *Suv39h1* KD causes delay in the development of Lp30 leukemia. (**A**) Schematic representation of the competitive assay used for validating SUV39H1 as a tumor-promoting factor in the Lp30 AML model. (**B**) Representative example of the in vivo depletion of *Suv39h1* KD (GFP-expressing) cells. (**C**) Left: Quantification of the data in (B). Right: KD efficiency with two different shRNAs quantified by quantitative reverse transcription polymerase chain reaction (qRT-PCR). (**D**) As in (C), but here, the recipients were transplanted with mixtures of freshly harvested bone marrow cells from primary recipients transplanted with sorted cells. (**E**) Survival of sublethally irradiated recipient mice injected with sorted cells transduced with either a *Suv39h1*-targeting shRNA or a scrambled control. Data in (C) and (D) were subjected to an unpaired *t* test, whereas data in (E) were subjected to a log-rank test. Asterisks indicate the following: $^{*}P < 0.05$; $^{**}P < 0.01$; $^{***}P < 0.001$; $^{****}P < 0.0001$. Each data point in (C) and (D) represents a biological replicate. Data in (C) illustrate a representative example of two independent experiments, whereas the experiments depicted in (D) and (E) were performed once.

The proliferation defects following depletion of SUV39H1 in U937 cells were accompanied by a decreased proportion of cells in S phase (Fig. 2B). To address this further, we treated U937 cultures with the mitosis inhibitor, nocodazole, and observed that *SUV39H1* KD cells, in contrast to control cells, failed to accumulate in the S-G_2-M phases of the cell cycle (Fig. 2C). This, in turn, suggests that the observed growth retardation is due to a cell cycle delay before mitotic entry, likely at the G_1-S phase transition. It has previously been reported that treatment of U937 cells with the pan-SUV39H inhibitor, chaetocin, results in S phase accumulation and massive numbers of apoptotic cells (*23*). Although we did observe a mild increase in the frequency of apoptotic cells following depletion of SUV39H1 (fig. S2B), the levels remained low (around 3%). This was despite the up-regulation of *FASL* (fig. S2C), which has been shown to be crucial for the apoptotic phenotype mediated by chaetocin (*23*). In Kasumi-1 cells, we also detected a decrease of cells in both the S and G_2-M phases following *SUV39H1* KD, although the effect on cells in G_2-M was only significant with one of the two shRNAs (fig. S2D). As for U937 cells, we observed increased levels of apoptotic cells (fig. S2E). Last, we assessed the extent to which depletion of SUV39H1 affected myeloid differentiation and found a mild but significant increase in the expression of the myelomonocytic marker, CD11b (Fig. 2D).

In summary, *SUV39H1* KD in U937 cells leads to growth retardation, most likely at the G_1-S phase transition. Our data also revealed marked phenotypic differences between the pan-SUV39H inhibitor, chaetocin, and the targeted depletion of SUV39H1.

Alterations in H3K9 trimethylation following SUV39H1 depletion do not correlate with gene expression changes

SUV39H1 is one of three HMTs responsible for trimethylation of H3K9. To understand the extent to which changes in H3K9me3 levels could explain the growth phenotype of *SUV39H1* KD cells, we first performed Western blot analysis on lysates from U937 cells, which had been either treated with different doses of chaetocin or transduced with shRNA-expressing retroviruses (Fig. 3A). In agreement

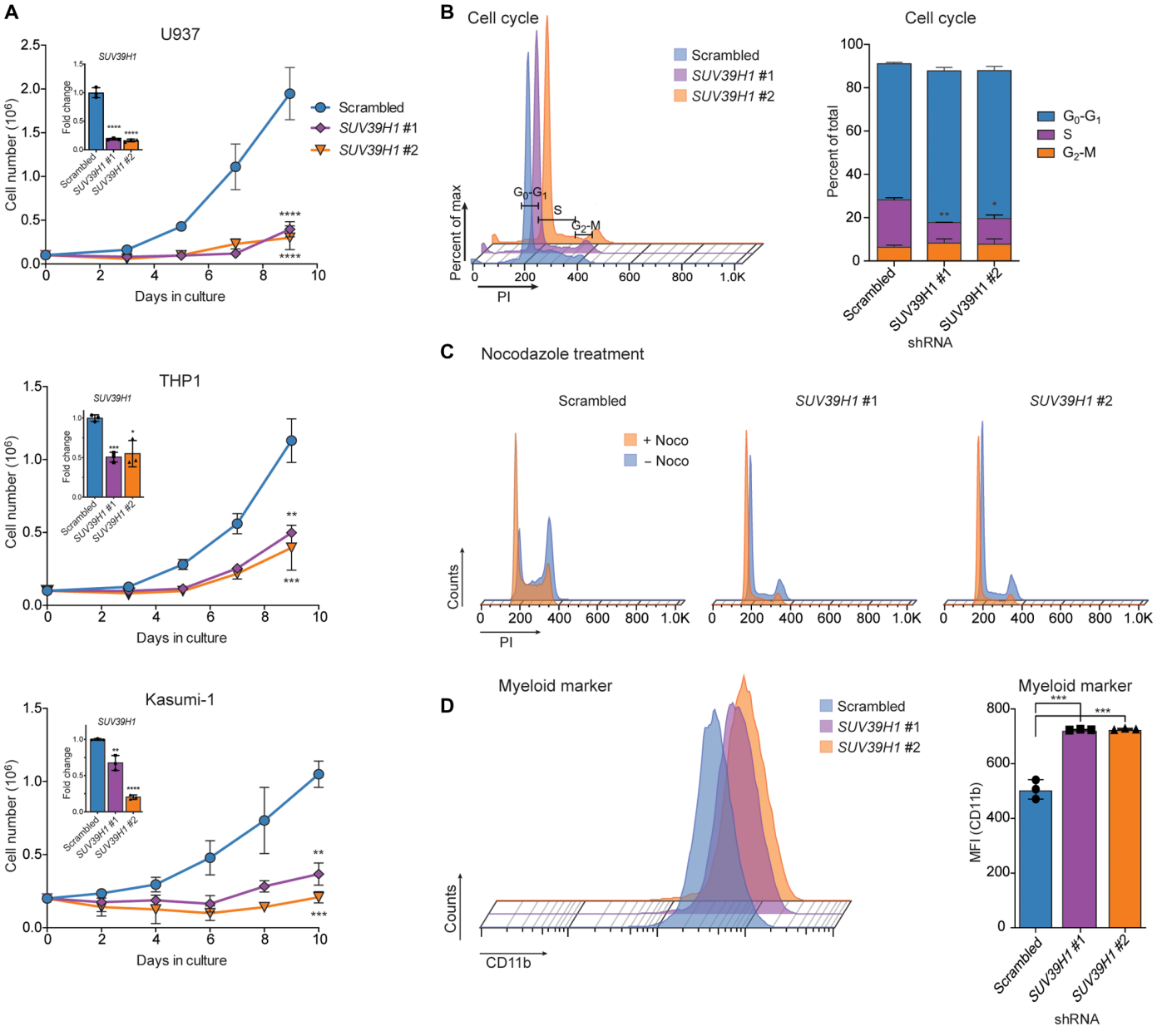

Fig. 2. *SUV39H1* KD causes growth arrest in human myeloid cells. (**A**) Growth of three different myeloid cell lines transduced with the indicated lentiviral shRNA constructs or scrambled controls. All transductions were carried out in triplicate, and KD efficiencies determined by qPCR are illustrated as insets. (**B**) Cell cycle analyses of *SUV39H1* KD U937 cells. Quantification of the relative number of cells in G_0-G_1, S, and G_2-M is shown in the right panel. The experiment was carried out in triplicate. PI, propidium iodide. (**C**) Effect of nocodazole treatment of U937 cells on cell cycle of cells transduced with the indicated SUV39H1 shRNA constructs or with a scrambled control. (**D**) Effect of transduction of U937 cells with the indicated SUV39H1 shRNA constructs or with a scrambled control on the expression of the myeloid cell surface marker, CD11b, as assessed by flow cytometry. Quantification is shown in the right-hand panel. Data in (A), (B), and (D) were subjected to an unpaired *t* test. Asterisks indicate the following: **P* < 0.05; ***P* < 0.01; ****P* < 0.001; *****P* < 0.0001. Each data point represents a biological replicate. Data in (A) illustrate a representative example of two independent experiments, and (B) to (D) each illustrates a representative example of three independent experiments.

with previous findings (*23*), we observed a dose-dependent decrease in the global levels of trimethylated H3K9 (H3K9me3) in response to chaetocin treatment. In contrast, *SUV39H1* KD had no effects on global H3K9me3 levels, implying that, if the observed phenotypic changes could be assigned to alterations in H3K9 trimethylation levels, these would have to occur on specific chromatin regions.

To potentially correlate alterations in H3K9me3 levels with gene expression changes following *SUV39H1* KD, we performed RNA sequencing (RNA-seq) and H3K9me3 chromatin immunoprecipitation sequencing (ChIP-seq) on U937 cells transduced as described above. To ensure that a sufficient sequencing depth was reached in the ChIP-seq analysis, we carried out saturation analysis confirming that the libraries had been sequenced at a sufficient depth to reach the maximal number of peaks (fig. S3A). RNA-seq analysis identified 2983 genes as significantly deregulated [$P_{adj} < 0.05$, fold change (FC) > 2] in response to both *SUV39H1*-targeting shRNAs (Fig. 3B

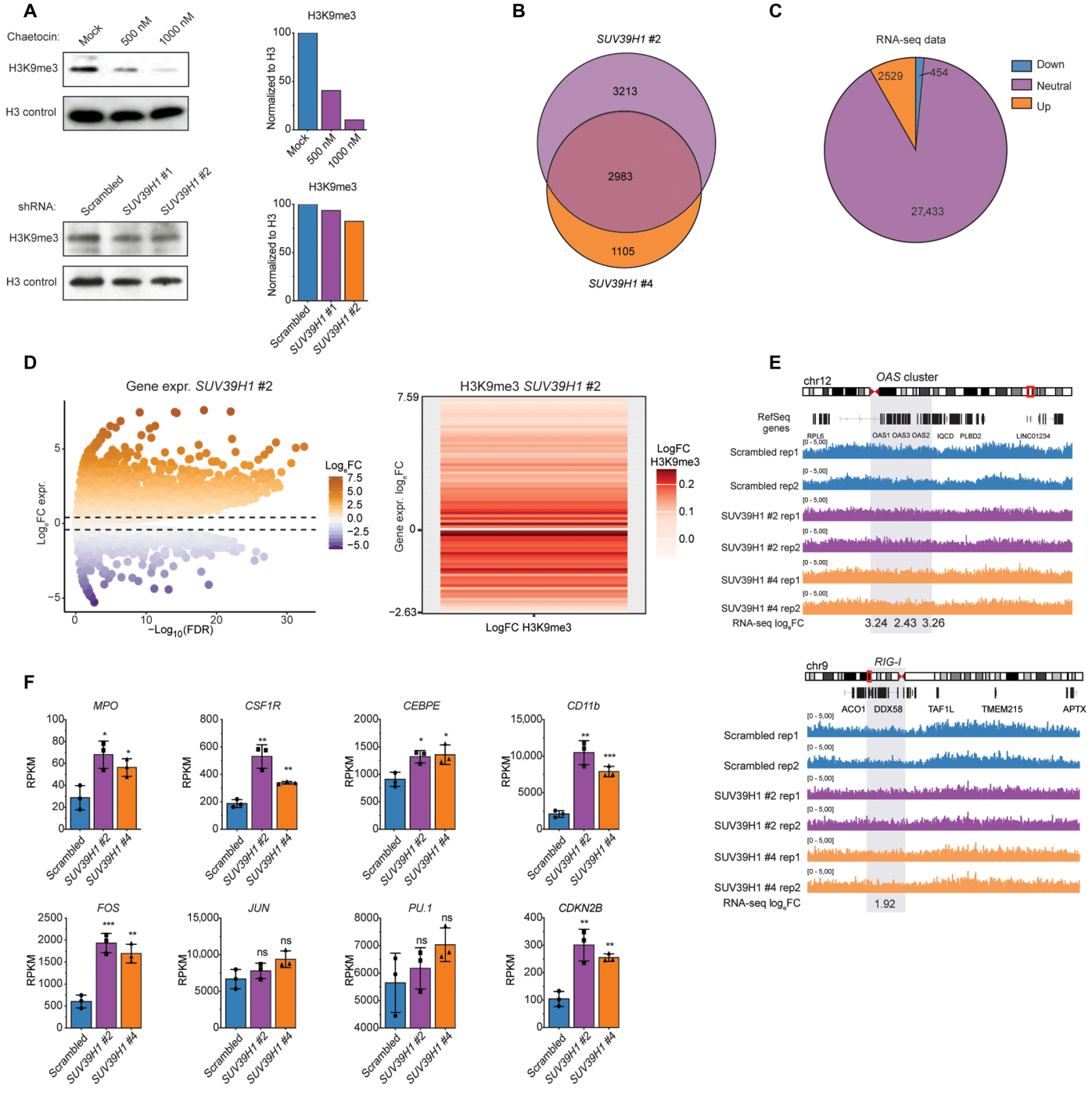

Fig. 3. Gene expression and epigenetic changes in U937 cells following depletion of *SUV39H1*. (**A**) Western blots showing levels of trimethylated H3K9 (H3K9me3) after chaetocin treatment (top) and *SUV39H1* KD (bottom). Quantifications are shown to the right, and total histone H3 was used as loading control. (**B**) Venn diagram illustrating the overlap of deregulated genes from RNA sequencing (RNA-seq) data derived from U937 cells transduced with two separate *SUV39H1*-targeting shRNAs. $P_{adj} < 0.05$, fold change (FC) > 2. (**C**) Distribution of down-regulated, up-regulated, or neutral genes overlapping between the two *SUV39H1*-targeting shRNAs in U937 cells. (**D**) Volcano plot illustrating deregulated genes after *SUV39H1* KD. The heatmap depicts the categories of up- or down-regulated genes (bins of 250 genes) and the changes in H3K9me3 coverage from TSS (Transcription start site) to TES (Transcription end site) of the corresponding gene bins. FDR, false discovery rate. (**E**) H3K9me3 chromatin immunoprecipitation sequencing (ChIP-seq) tracks illustrating the *OAS* cluster and the *RIG-I* gene. (**F**) Examples of genes with deregulated expression [in reads per kilobase per million reads (RPKM) from the RNA-seq data] after *SUV39H1* KD. Data in (F) were subjected to an unpaired *t* test. Asterisks indicate the following: **P* < 0.05; ***P* < 0.01; ****P* < 0.001. Data in (A) and (F) illustrate a representative example of two independent experiments. ns, not significant.

and data files S1 to S3). Of these, 2529 genes were up-regulated, whereas only 454 genes were down-regulated (Fig. 3C and data file S4). To correlate changes in H3K9me3 and gene expression, we ordered ChIP-seq H3K9me3 reads spanning gene bodies in segmental bins of 250 genes according to the corresponding $\log_e$FC gene expression levels after *SUV39H1* KD. Notably, this analysis did not reveal any clear association between alterations in intragenic H3K9 trimethylation and mRNA expression following *SUV39H1* KD (Fig. 3D). Concordantly, a pairwise comparison of changes in expression of versus H3K9 on individual genes revealed only a weak anticorrelation (fig. S3B). This is exemplified by genes that are highly induced in response to *SUV39H1* KD but do not display any detectable changes in H3K9me3 (Fig. 3E and data file S3).

In short, *SUV39H1* KD did not result in global changes in H3K9me3 levels and we did not observe any major correlation between local changes in H3K9me3 levels and mRNA expression. Therefore, these findings do not support a role for H3K9me3 in driving the phenotypic changes associated with loss of SUV39H1.

The growth phenotype of SUV39H1 depletion depends on induction of interferon pathway genes

Consistent with a myeloid differentiation phenotype, the RNA-seq analysis revealed that a number of myeloid determinants, including CD11b, *CEBPE*, *CSF1R*, and *MPO*, were up-regulated following *SUV39H1* KD (Fig. 3F and data file S3). In line with previous observations (*16*), we also found a modest increase in the expression of *CDKN2B*, encoding the tumor suppressor p15, whereas other factors previously associated with SUV39H1 dependence in AML cell lines were not affected (Fig. 3F and data files S2 and S3).

To obtain a more global picture of the gene expression changes associated with *SUV39H1* KD, we performed gene set enrichment analysis (GSEA). This revealed a notable up-regulation of genes involved in viral defense pathways such as pattern recognition receptors (PRRs) and other IFN type I–associated pathway components (Fig. 4A and data file S6). Given the potential implications of IFN pathway activation in cancer treatment, we focused our attention on these pathways. Specifically, we verified the up-regulation of genes encoding 2′-5'-oligoadenylate synthetase (OAS) 1 to 3, retinoic acid–inducible gene (RIG) I, and melanoma differentiation–associated gene (MDA) 5, which are all PRRs that, after binding of dsRNA, mediate an IFN response via downstream effectors (Fig. 4, B and C) (*29*–*32*). These PRRs were also up-regulated in THP-1 cells in response to *SUV39H1* KD (fig. S3C).

The mitochondrial antiviral signaling protein (MAVS) is a central hub in type I IFN signaling and acts downstream of all the up-regulated PRRs (Fig. 4C). Thus, to address the functional importance of IFN signaling as a driver of the growth inhibitory effect in U937 cells, we tested whether depletion of MAVS could rescue the *SUV39H1* KD phenotype. Consistent with a prominent role of type I IFN signaling in mediating the growth inhibitory phenotype, depletion of MAVS led to a marked rescue of proliferation (Fig. 4D). Last, to test the possibility that paracrine signaling may also play a role in driving the expression of IFN-stimulated genes (ISGs) in neighboring cells, we treated nonperturbed U937 cells with conditioned media from *SUV39H1* KD cells. We found that the conditioned medium from *SUV39H1* KD cells contained elevated levels of IFN-α and that it promoted the expression of ISGs in unperturbed U937 cells (Fig. 4, E and F). However, we did not observe any significant effect on cell growth after subjecting U937 to *SUV39H*1 KD supernatant (fig. S3D), demonstrating that while the induced expression of IFN pathway genes contributes to the observed growth retardation and gives rise to a paracrine response, the latter is not sufficient to affect growth of unperturbed cells.

Collectively, these findings suggest that the loss of SUV39H1 promotes the activation of type I IFN signaling, leading to growth inhibition, and that the activation spreads between cells. This phenotype does not appear to be driven by changes in H3K9me3 at the involved genes.

SUV39H1 KD results in G9A/GLP destabilization, decreased deposition of H3K9me2, and induction of the IFN pathway

The aforementioned lack of correlation between H3K9me3 levels and gene expression changes, including those occurring at IFN pathway genes, suggests that the phenotypes associated with depletion of SUV39H1 were separated from its canonical enzymatic activity. SUV39H1 exists in a protein complex with G9A and its homolog GLP, in which complex formation facilitates the stabilization of the individual components (*17*). G9A and GLP are two HMTs that are responsible for the generation of H3K9me2, a repressive mark associated with euchromatin. Low levels of H3K9me2 are crucial for the ability of dendritic cells to orchestrate an IFN response, and *G9A* knockout (which results in grossly decreased global H3K9me2 levels) in otherwise IFN-unresponsive fibroblasts renders these cells hyperresponsive to polyI:C-induced IFN induction (*31*). These findings raise the possibility that SUV39H1 supports tumor growth by stabilizing G9A/GLP, which, in turn, ensures that the IFN pathway genes are kept in check by H3K9me2-mediated repression.

To test whether *SUV39H1* KD affects the levels of G9A and GLP, we performed Western blotting on U937 cells transduced with *SUV39H1*-targeting shRNAs (at this point, we switched from shRNA #1 to #4 during the project because we obtained a more robust KD with the latter). Consistent with a putative stabilizing role of SUV39H1, its depletion led to markedly decreased G9A/GLP levels and an accompanying global decrease in H3K9me2 (Fig. 4G). To assess whether this effect was driving the antiproliferative phenotype of *SUV39H1* KD, we next performed a mimicking experiment using G9A-targeting shRNAs. We found that *G9A* KD resulted in growth impairment; however, the effect was less dramatic than that observed following depletion of SUV39H1 (fig. S3E). Concordantly, we observe neither the same global decrease of H3K9me2 (Fig. 4G) nor the same degree of induction of IFN pathway genes (compare Fig. 4B and fig. S3F). A potential explanation for the latter observation is that *G9A* KD might be less efficient than *SUV39H1* KD in reducing total G9A/GLP levels.

Similar to human cells, *Suv39H1* KD in murine MLL-AF9 cells led to a slight decrease in global H3K9me2 levels (fig. S3G); however, this was not accompanied by any increase in the expression of IFN pathway genes, in surface expression of the myeloid marker Mac-1 or in apoptotic cells after KD (fig. S3, H to J). This finding is in good agreement with the milder proliferation phenotype of *Suv39H1* KD MLL-AF9 cells compared to the human cell lines used in this study (fig. S1D), suggesting that either IFN pathway induction in MLL-AF9 cells is below the sensitivity of the assay or the remaining proliferation phenotype is mediated via other mechanisms. To address this further, we used CRISPR-mediated targeting to down-regulate SUV39H1 in MLL-AF9 cells. In this context, the reduction in proliferation (fig. S3K) was associated with a more pronounced decrease in global H3K9me2 levels [compare fig. S3 (G and L) for shRNA and CRISPR-mediated down-regulation, respectively] and in the induction of IFN genes such as

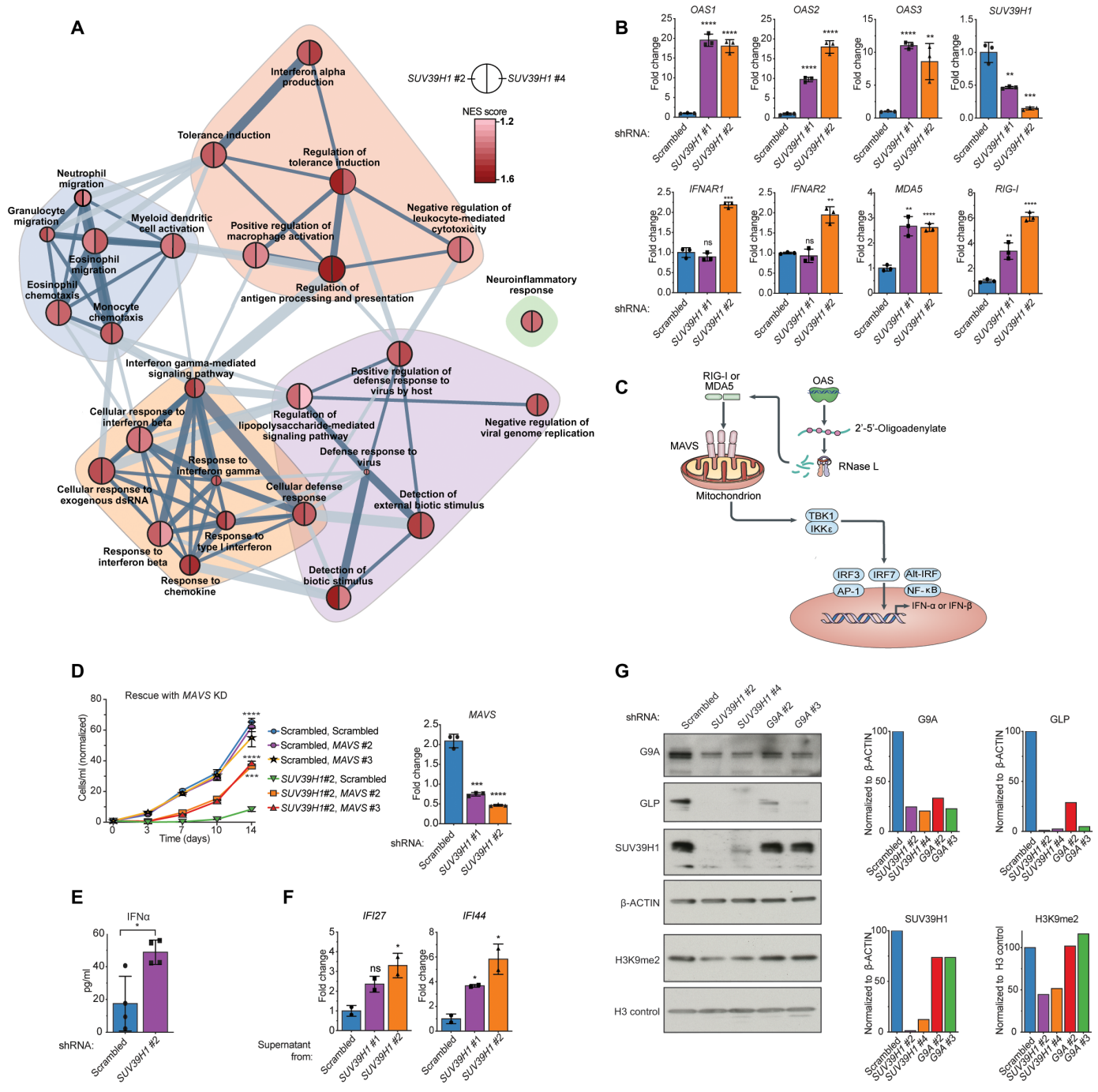

Fig. 4. Activation of IFN pathway genes after *SUV39H1* KD. (**A**) Illustration of a GSEA analysis network performed on Scrambled versus *SUV39H1* KD in U937 cells after 4 days of selection. The network is generated on overlapping Gene Ontology (GO) terms with significant normalized enrichment scores (NES) from GSEA analysis. The network is visualized by R igraph package, whereas the node size represents the number of genes per GO term and the edge width represents the number of overlapping genes between GO terms. Edges with >20% similarity between nodes are kept. Node pie color corresponds to NES score. (**B**) qRT-PCR of the PRRs *OAS1* to *OAS3*, *RIG-I*, and *MDA5* as well as *IFNAR1* and *IFNAR2* before and after *SUV39H1* KD (3 days after selection). (**C**) Schematic representation of a simplified type I IFN pathway. MAVS, mitochondrial antiviral signaling protein; OAS, 2′-5′-oligoadenylate synthetase; RIG-I, retinoic acid–inducible gene I; MDA5, melanoma differentiation–associated gene 5; IRF3, IFN regulatory factor 3; NF-κB, nuclear factor κB; RNase, ribonuclease. (**D**) Rescue of the growth phenotype in U937 cells after *MAVS* KD in *SUV39H1* KD cells. KD efficiency of *MAVS* 3 days after transduction is shown in the right panel. (**E**) Enzyme-linked immunosorbent assay assessing IFN-α levels in the supernatant from U937 cells 3 days after transduction with Scrambled or *SUV39H1*-specific shRNA constructs. (**F**) qRT-PCR of *IFI27* and *IFI44* mRNA levels in U937 cells subjected to supernatant from Scrambled or *SUV39H1* KD cells for 24 hours. (**G**) Left: Western blot of proteins in the HMTs complex and the H3K9 dimethylation levels after 3 days of *SUV39H1* and *G9A* depletion. Right; Protein quantification using ImageJ. G9A, GLP, and SUV39H1 were normalized to β-actin and H3K9me2 to H3 control. Data in (B) and (D) to (F) were subjected to an unpaired *t* test. Asterisks indicate the following: **P* < 0.05; ***P* < 0.01; ****P* < 0.001; *****P* < 0.0001. Each data point in (B) and (D) to (F) represents a biological replicate. Data in (A), (C), (D), and (G) illustrate a representative example of two independent experiments, whereas the experiments depicted in (E) and (F) were performed once.

Oas1g, *Oas1m*, *Oas2*, and *Oas3*, which was absent after shRNA-mediated KD (fig. S3M). Hence, these analyses correlate the extent of H3K9me2 loss to the induction of key IFN pathway genes.

To summarize, we found that SUV39H1 stabilizes the homologous HMTs G9A and GLP, thereby ensuring deposition of the repressive mark, H3K9me2, normally repressing the expression of IFN pathway genes, which would otherwise lead to growth retardation.

Pharmacological inhibition of G9A/GLP results in an IFN response similar to SUV39H1 KD

To further assess the extent to which down-regulation of H3K9me2 levels mediates the phenotypic consequences of *SUV39H1* KD, we next treated U937 cells with UNC0638, an inhibitor that blocks the enzymatic activities of the SET domains of both G9A and GLP (*33*). Mimicking the phenotypic consequences of *SUV39H1 KD*, this treatment resulted in a dose-dependent growth inhibition induction of IFN pathway genes and loss of H3K9me2 (Fig. 5, A to C). To assess the dynamics of this process, we performed a time course experiment demonstrating that induction of *OAS1* expression did not become clearly evident before 3 days of treatment (fig. S4A). Given that the global effect on H3K9me2 levels is observed already after 2 days (Fig. 5C), this suggests that induction of *OAS1* expression is dependent on the loss of the H3K9m2 repressive mark.

Similar effects on growth, IFN response, and H3K9me2 levels were also observed in THP-1 cells (fig. S4, B to D), whereas an inhibitory effect was observed on in vitro growth of primary AML samples, but not on nonmalignant human bone marrow cells (fig. S4E). Moreover, UNC0638 did not affect the levels of G9A or SUV39H1, demonstrating that the functional inhibition of G9A/GLP activities is sufficient to result in phenotypic consequences. Last, the UNC0638-induced growth phenotype could be partly rescued by *MAVS* KD, demonstrating again that induction of IFN pathway genes is underlying the phenotype (Fig. 5D). The *MAVS* KD-induced rescue of the UNC0638 phenotype was less prominent than in the *SUV39H1* KD setting (compare Figs. 5D and 4D), which correlates with the less pronounced induction of *OAS* genes in the former case.

To compare the transcriptional effects of G9A/GLP inhibition to those of *SUV39H1* KD, we next performed RNA-seq on U937 cells treated with either 2 or 4 μM G9A/GLP inhibitor and identified 844 genes to be commonly deregulated between the two conditions (fig. S4F and data files S3 to S5). Of these, 755 genes were up-regulated and only 89 genes down-regulated, consistent with removal of a repressive histone mark (fig. S4G and data file S5). Supporting the notion that G9A/GLP inhibitor treatment mimics the *SUV39H1* KD phenotype, GSEA revealed an enrichment of the same IFN pathway gene sets as those detected following *SUV39H1* KD (Fig. 5E and data file S6). In addition, we observed an overlap of 372 up-regulated genes between the two conditions (fig. S4H and data file S5).

Next, we wanted to assess the extent to which H3K9me2 correlated with gene expression changes and therefore performed ChIP-seq using antibodies against H3K9me2 in U937 cells treated with the G9A/GLP inhibitor. As for H3K9me3, we carried out saturation analysis to ensure that the library had been sequenced to a sufficient depth (fig. S4I). In agreement with the global changes in H3K9me2 levels, this analysis revealed a dose-dependent global decrease in H3K9me2 levels at gene bodies following UNC0638 treatment (fig. S4J). Contrary to what we observed for the H3K9me3 mark, we now detect a strong negative correlation between gene expression and the changes in the H3K9me2 mark (Fig. 5F). At the levels of individual genes, we observed a clear decrease in the H3K9me2 mark on the gene bodies of up-regulated IFN pathway genes, including the OAS cluster and RIG-I (Fig. 5, G and H). This finding could be expanded to THP-1 cells, where ChIP quantitative polymerase chain reaction (qPCR) revealed a significant decrease in H3K9me2 decorating the gene bodies of selected IFN pathway genes after UNC0638 treatment (fig. S4J).

To directly assess the combined effect of targeting both *G9A* and *GLP*, we knocked down both factors and found an additive effect on cell proliferation and *OAS1* expression compared to the individual KDs (fig. S4, L and M). Similar to the *G9A* single KD, we found no global changes in H3K9me2 (fig. S4N). However, in concordance with the observed effect on OAS1 expression, ChIP-qPCR revealed a small but significant loss of the mark on *OAS1*, *OAS2*, and *IFIT4* (fig. S4O). The notion that even *G9A/GLP* double KD has a weaker phenotype than *SUV39H1* KD or the pharmacological inhibition of G9A/GLP inhibition could be explained either by an insufficient KD of the two targets or by the existence of one or several H3K9-specific methyl transferases that mediate dimethylation, which are also targeted by UNC0638. Potential candidates for the latter are PRDM2 and PRDM8, which have been demonstrated to confer H3K9 dimethylation (*34*, *35*).

Last, to further substantiate that the effect of *SUV39H1* KD on IFN pathway gene expression also occurs via loss of H3K9me2 (and thus is mechanistically linked to the effect of G9A/GLP inhibition), we performed ChIP-qPCR and found *SUV39H1* KD to be associated with a significant loss of H3K9me2 on *OAS1*, *OAS2*, and *IFIT4* (fig. S4P).

Collectively, G9A/GLP inhibition closely mimicked the phenotype and gene expression profile resulting from *SUV39H1* KD. Changes in H3K9me2 levels correlated inversely with gene expression. Although the latter is not specific to IFN pathway genes, the functional importance of this pathway for cell growth as demonstrated here suggests that the H3K9me2 mark constitutes a major safeguard in cancer cells against untimely expression of IFN gene.

Derepression of retrotransposons synergizes with G9A/GLP targeting in promoting growth inhibition

It has previously been demonstrated that treatment of various tumor cell lines with DNMTis, such as 5-azacytidine (5-AZA), results in an IFN response induced by the derepression of retrotransposon-derived dsRNA; triggering of PRRs like OAS, RIG-I, and MDA5; and, ultimately, impairment of tumor growth (*18*, *19*). Given that H3K9me3 and DNA methylation collaborate in repressing the expression of retrotransposons, we hypothesized that down-regulation of SUV39H1 might also alleviate their repression. qPCR as well as RNA-seq analysis revealed that *SUV39H1* KD in U937 cells promoted the mild transcriptional up-regulation of the three subclasses of retrotransposons [ERVs (Endogenous retroviruses), LINEs, and SINEs (Short interspersed nuclear elements); fig. S5, A and B]. To test the possibility that this up-regulation is a direct consequence of loss of H3K9me3, we identified individual repeat elements overlapping with H3K9me3 peaks and compared changes in the H3K9me3 peak levels with RNA expression from the elements (fig. S5C). However, this analysis revealed weak or no anticorrelations between changes in mRNA expression and H3K9me3 levels on these elements. Next, to test the possibility that the transcriptional activation is mediated via loss of interactions between SUV39H1 and factors mediating DNA methylation (*36*), we performed whole-genome bisulfite sequencing.

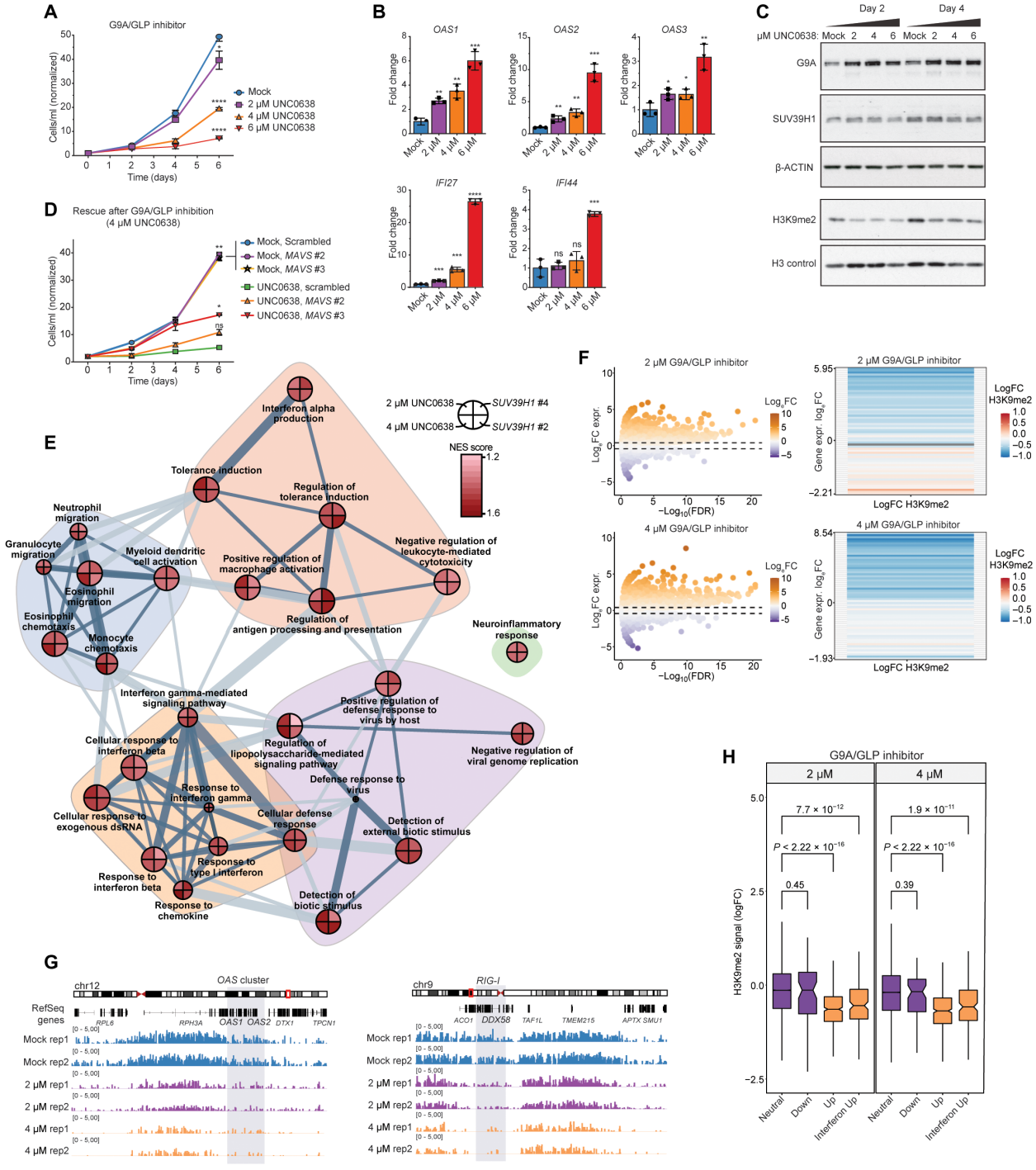

Fig. 5. Pharmacological G9A/GLP inhibition mimics the phenotype and IFN response as in *SUV39H1* KD. (**A**) Growth of U937 cells after UNC0638 treatment. (**B**) qRT-PCR quantification of mRNA encoding the PRRs *OAS1* to *OAS13* and ISGs *IFI27* and *IFI44*, after treatment with UNC0368 at the indicated concentrations for 3 days. (**C**) Western blot showing the levels of G9A, SUV39H1, β-actin, H3K9me2, and total histone H3 in U937 3 days after treatment with UNC0368 at the indicated concentrations. (**D**) Rescue of UNC0368-mediated growth retardation of U937 cells after *MAVS* KD. (**E**) GSEA network from Fig. 4B onto which the GSEA data for the corresponding signatures, derived from UNC0638-treated U937 cells, are superimposed. (**F**) Volcano plot of deregulated genes in response to UNC0638 treatment. The heatmap illustrates bins of genes (250 genes per bin) based on Log_eFC gene expression (*y* axis) and the coverage of H3K9me2 from TSS to TES on the binned genes. (**G**) H3K9me2 ChIP-seq tracks on PRRs (*OAS* cluster and *RIG-I*) after 3 days of UNC0638 treatment. The tracks are normalized to reads derived from the *Drosophila* spike-in. (**H**) Quantification of H3K9me2 reads from TSS to TES on neutral, up-, and down-regulated genes after G9A/GLP inhibitor treatment, as well as IFN genes significantly up-regulated in response to both UNC0638 treatment. The IFN genes were determined by INTERFEROME v2.0 (*62*). Each data point in (B) represents a biological replicate. Data in (A), (B), and (D) were subjected to an unpaired *t* test. Asterisks indicate the following: **P* < 0.05; ***P* < 0.01; ****P* < 0.001; *****P* < 0.0001. Data in (H) were subjected to a one-tailed Wilcox test, and *P* values are indicated on the graph. Data are representative of two independent experiments (A to C) or one independent experiment (D).

As expected, this analysis revealed a slight decrease in CpG methylation on all three classes of retrotransposons after *SUV39H1* KD, albeit with no specificity for up-regulated genes (fig. S5D). Together, these findings suggest that SUV39H1 KD exerts its effects on retrotransposon transcription via local epigenetic alterations, which cannot be precisely mapped due to the repetitive nature of these elements.

Despite the overlapping phenotypes of *SUV39H1* KD and G9A/GLP inhibitor treatment (IFN pathway induction and growth inhibition), the latter did not result in the transcriptional up-regulation of retrotransposons (fig. S6A). Not only did these findings demonstrate the specific role of SUV39H1 in the repression of retrotransposon expression, but they also raised the possibility that this might add to the growth inhibitory potential of the G9A/GLP inhibitor UNC0638.

To test this hypothesis, we treated U937 cells with combinations of UNC0638 and 5-AZA, a DNMTi widely used in the treatment of AML and myelodysplastic syndrome (*37*). Our setup included an initial 3-day treatment with different concentrations of 5-AZA followed by 3 days of combined treatment with 5-AZA and UNC0638. Cell numbers were used to calculate a zero interaction potency (ZIP) score (*38*), where a score > 0 is defined as a synergistic effect between the two drugs. We observed a general synergy score of 13.03 and a peak score of 20.34 at concentrations of 0.1 μg/ml and 6 μM, respectively, of 5-AZA and UNC0638 (Fig. 6A and fig. S6B). Consistent with a role for retrotransposons in synergizing with reduced H3K9me2 levels, prolonged treatment with 5-AZA alone induced the expression of these heterochromatic elements (fig. S6C) and, in concordance with the hypothesis that the growth inhibition is mediated by expression of IFN pathway genes, the two drugs displayed a strong synergistic effect in activating the expression of OAS1 and IFI27 (Fig. 6B).

To assess whether a similar synergy can be achieved by simultaneous impairment of SUV39H1 activity and DNA methylation, we treated U937 cells with 5-AZA in combination with chaetocin and used cell numbers to calculate the ZIP score between 5-AZA and chaetocin. As shown in fig. S6D, a maximum synergy score of 33 was observed at concentrations of 0.1 μg/ml and 5 μM, respectively, of 5-AZA and chaetocin. These findings suggest that simultaneous DNA demethylation and inhibition of H3K9me3 activity is highly antiproliferative.

To assess the clinical relevance of our observations, we next used publicly available AML patient data to gauge how *SUV39H1* levels affected patient outcome (*39*). Consistent with our experimental findings, we observed an inverse relationship between *SUV39H1* expression and clinical outcome in patients treated with hypomethylating agents in combination with low-dose cytarabine (Fig. 6C, left). In contrast, no significant effect of *SUV39H1* expression could be detected when assessing the survival of all patients from the same study (Fig. 6C, right). Further supporting the notion that the differential treatment response depends on IFN pathway genes, we observed an inverse correlation between expression of *SUV39H1* and *OAS-1*, *OAS-2*, and *RIG-I* (Fig. 6D).

In contrast, we did not observe any link between *G9A/GLP* expression and survival—neither for patients treated with hypomethylating agents and cytarabine nor for all patients regardless of treatment regime (fig. S6E). The lack of an obvious correlation is in good concordance with our in vitro data, demonstrating a less pronounced effect on both cell proliferation and IFN gene induction following *G9A* KD as compared to depletion of SUV39H1. Collectively, our data suggest that combinatorial treatment strategies aimed at targeting both H3K9 dimethylation and DNA methylation may have clinical potential in AML—and perhaps also in other cancer types.

DISCUSSION

Targeting of epigenetic regulators constitutes an interesting therapeutic option for the treatment of cancer. This is both because of their frequent deregulation of the epigenome in cancer and because many of these changes are potentially reversible. Moreover, epigenetic regulators frequently harbor enzymatic activities and are consequently amenable to inhibition by small molecules.

Although the requirement of the H3K9me3 HMT SUV39H1 has been demonstrated in various cancer types, the underlying mechanisms have remained obscure. In the present study, we demonstrate inhibitory effects of SUV39H1 on apoptosis and myeloid differentiation. This has potential clinical relevance since induction of these processes is already being used in standard treatment of myeloid malignancies with agents such as venetoclax and all-trans retinoic acid (ATRA). At the mechanistic level, we demonstrated that a key oncogenic property of SUV39H1 is its function as a stabilizer of a large protein complex. This complex also contains the HMTs G9A and GLP, which are responsible for depositing the repressive mark H3K9me2 on euchromatin, including regions comprising IFN pathway genes (Fig. 6E) (*31*). We show that the ablation of the ability of this complex to deposit H3K9me2, either by depleting SUV39H1 or by inhibiting the enzymatic activity of G9A/GLP, resulted in the activation of IFN pathway genes. This most likely occurs via the up-regulation of the PRRs OAS, RIG-I, and MDA5 and subsequent activation of the MAVS signaling pathway, ultimately leading to growth inhibition (Fig. 6E, top and middle). This effect could be further enhanced by treatment with the DNMTi, 5-AZA, which, in accordance with previous reports, also mediates derepression of heterochromatin-associated retrotransposons (*19*). The resulting bidirectional (and thus double-stranded) transcripts are likely to further increase activation of the PRRs and therefore result in an enhanced IFN response (Fig. 6E, bottom).

Earlier work has implicated G9A/GLP as proteins required for AML proliferation and as repressors of factors involved in IFN pathway activation, such as Janus kinase 2 (*40*–*44*). Furthermore, a strong effect of the combined interference with G9A/GLP and DNMT1 activities has been demonstrated in colon and ovarian cancer cells (*45*, *46*). Here, the two modalities promoted the synergistic induction of IFN pathway genes and ERVs, which is consistent with an induction of these elements after G9A inhibition in bladder cancer cells (*47*). However, while the authors nicely linked the synergy on ERVs to a combined loss of H3K9me2 and DNA methylation directly on these elements, the potential link between H3K9me2 and the induction of IFN pathway genes was not assayed in this cellular context. Thus, to our knowledge, the present study is the first to demonstrate a direct functional link between G9A/GLP activity, IFN pathway activation, and proliferation of AML cells.

Previous work has highlighted DNA methylation as an important mechanism to safeguard cancer cells against the untimely expression of IFN pathway genes (*18*–*20*). Specifically, unleashing the expression of dsRNA from heterochromatin-associated retrotransposons by treatment with DNA demethylating agents activates RIG-1 or MDA5, leading to their colocalization with MAVS at

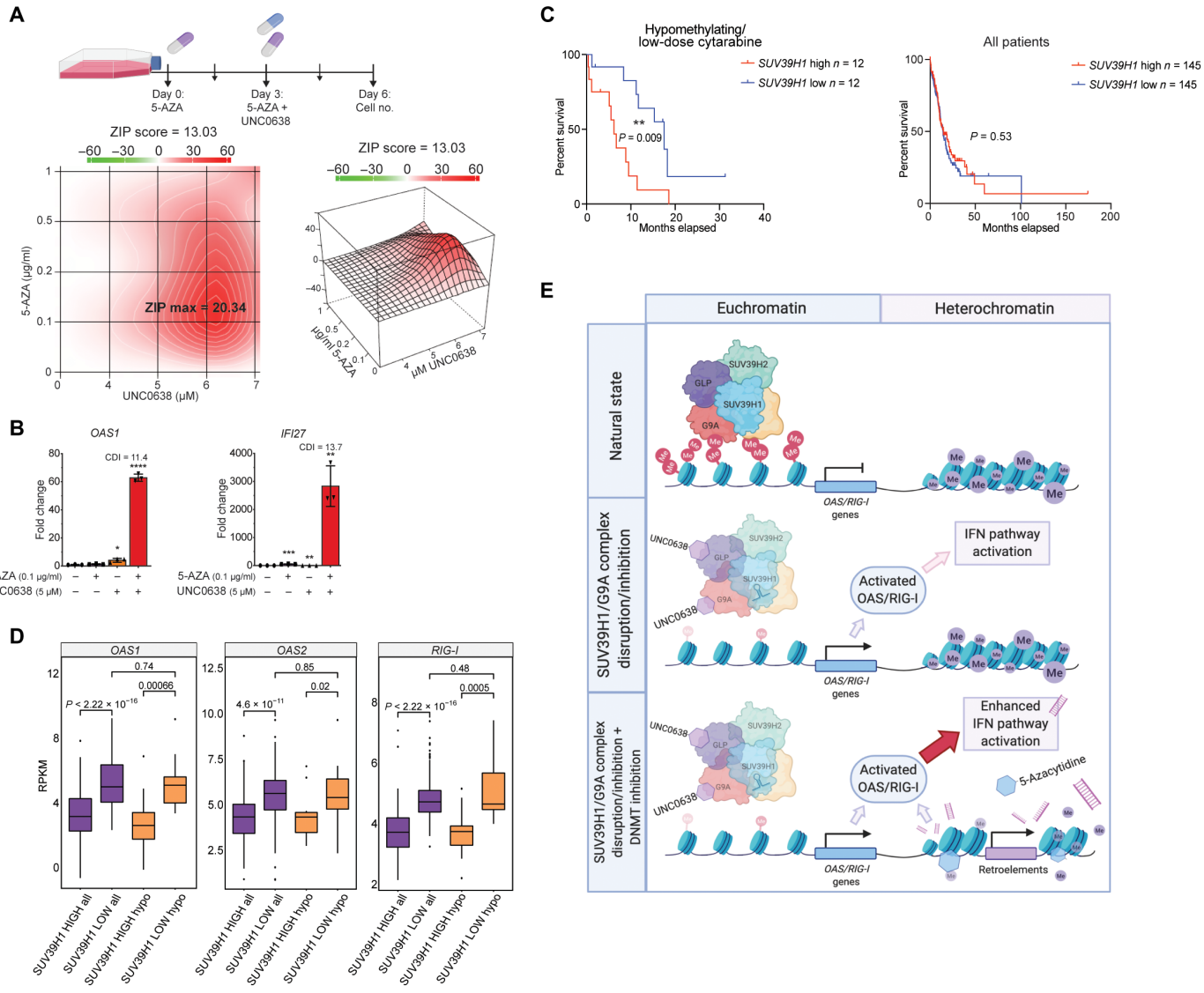

Fig. 6. Synergistic effect of dual inhibition of G9A/GLP and DNA methylation. (**A**) Dual treatment with the indicated doses of 5-AZA and UNC0638 in U937 cells. After 3 days of pre-incubation with 5-AZA, UNC0638 was added to the cells. On day 6, cells were counted and the synergy ZIP score was calculated by synergyfinder (*61*). (**B**) Effect of dual 5-AZA/UNC0638 treatment of U937 cells on *OAS1* and *IFI27* mRNA expression compared to treatment with the individual agents. Coefficient of drug interaction (CDI) is indicated for each target gene. (**C**) Left: Overall survival of patients with AML treated with hypomethylation agents and low-dose cytarabine stratified based on the levels of *SUV39H1* (high/low = top/bottom 40%); $n = 24$. Right: The same analysis performed on the entire dataset, irrespective of treatment ($n = 290$). Data were derived from (*39*). (**D**) RPKM of different PRRs expressed in patients with AML (all) based on *SUV39H1* expression and in patients treated with hypomethylating agents/ low-dose cytarabine [as in (C)]. (**E**) Model illustrating the unperturbed state with an intact HMT complex responsible for silencing of IFN pathway genes on euchromatin. Abrogation of SUV39H1 levels or interference with the enzymatic activities of G9A/GLP results in reduced H3K9me2 on IFN pathway genes. As a consequence, several PRRs, including OAS and RIG-I, are derepressed and the IFN type I pathway is activated. Additional treatment with DNMTis (5-AZA) (or if SUV39H1 is depleted) results in expression of retrotransposons (including viral dsRNA), which can further enhance cell death through an additional stimulation of the IFN pathway. Data in (B) were subjected to an unpaired *t* test. Data in (C) were subjected to a Mantel-Cox test. Data in (D) were subjected to a one-tailed Wilcox test, and *P* values are indicated on the graph. Asterisks indicate the following: $*P < 0.05$; $**P < 0.01$; $***P < 0.001$; $****P < 0.0001$. Data in (A) and (B) are representative of one independent experiment.

mitochondria. This, in turn, triggers a signaling cascade leading to the nuclear translocation of nuclear factor κB as well as IFN regulatory factor 3 (IRF3) and IRF7, and hence in type 1 IFN expression. Similar to RIG-I and MDA-5, OAS family members are also activated by dsRNA. Activated OAS catalyzes the formation of 2′-5′–linked oligoadenylate, which, in turn, activates ribonuclease (RNase) L, resulting in degradation of viral and endogenous mRNAs and hence inhibition of viral propagation and induction of apoptosis (*30*). In addition to this direct pathway, the aforementioned RNA degradation products have also been shown to bind and activate RIG-I and MDA-5 (Fig. 4C) (*48*, *49*). Thus, activation of either RIG-I/MDA5 or OAS family members can drive the IFN pathway activation.

Our work clearly establishes that the above-mentioned PRRs, and consequently the IFN pathway, may also be activated by an alternative pathway, specifically via the interference with the activities of enzymes responsible for deposition of H3K9me2. Direct interference

with the H3K9me2 levels by treatment with the G9A/GLP inhibitor, UNC0638, reduced the levels of H3K9me2 levels on key PRR genes such as OAS/RIG-I/MDA5, likely promoting their derepression and subsequent IFN pathway activation. Central to this alternative pathway of PRR activation is the multicomponent complex containing SUV39H1, G9A, and GLP. Abrogation of *SUV39H1* levels by shRNA-mediated KD destabilizes G9A and GLP, thus providing a mechanistic explanation for the reduction of H3K9me2 levels that we observed in this context. Changes in H3K9me2 levels were highly correlated with changes in gene expression, strongly suggesting that this epigenetic mark constitutes an important safeguard against activation of the IFN pathway. Our rescue experiments in the context of murine MLL-AF9 AML demonstrated that the *Suv39h1* KD phenotype could be rescued by WT SUV39H1 but not by the enzymatic dead version. Earlier biochemical experiments demonstrated that the stability of the SUV39H1/G9A/GLP complex is dependent on the catalytic activity of SUV39H1 and not on the mere presence of the protein (*17*). While this clearly establishes the importance of the catalytic function of SUV39H1, it is not clear why this is required for the maintenance of the SUV39H1/G9A/GLP complex. The formal possibility remains that some of SUV39H1 nonhistone targets may be required for this (*50*). Collectively, these findings firmly uncover the existence of an alternative mode of activation of the IFN pathway.

While SUV39H1 and G9A/GLP inhibition converge at down-regulation of H3K9me2 levels, *SUV39H1* KD also leads to the derepression of retrotransposon elements. We noted that the phenotypic consequences of interference with SUV39H1 appeared more severe (as measured by the number of deregulated genes and impact on growth) compared to those observed following pharmacological interference with G9A/GLP activity. The requirement of SUV39H1 in restricting the expression of retrotransposons in cancer cells likely reflects the general hypomethylated state of cancer genomes, which, in turn, makes retrotransposons more susceptible to derepression in case of interference with heterochromatin-associated H3K9me3. The selective sensitivity of cancer cells to depletion of H3K9me3 parallels observations from ESCs and their immediate derivatives (*20*). The clinical relevance of the interplay between H3K9me3 and DNA methylation is clearly established by our analysis of patients with AML receiving hypomethylation agents. Specifically, we find that low *SUV39H1* mRNA levels in this cohort were associated not only with the increased expression of PRRs but also with increased survival. These findings strongly suggest that assessment of *SUV39H1* levels could be used as a biomarker for selecting patients for treatment with hypomethylating agents such as 5-AZA.

Our work suggests that SUV39H1 is a potential actionable target in AML. However, current inhibitors, such as chaetocin, target both SUV39H1 and SUV39H2, likely resulting in collateral damage in normal cells. Here, we demonstrated that the effects of SUV39H1 down-regulation (derepression of retrotransposons and down-regulation of H3K9me2 levels) could be mimicked pharmacologically (and exacerbated) by combining 5-AZA with the G9A/GLP inhibitor, UNC0638. The synergistic effects of these drugs that we observe argue for the potential of combining agents targeting DNA methylation and H3K9me2 in future cancer treatment strategies.

In conclusion, we have shown that both H3K9me2 and H3K9me3 HMTs are important for protecting cancer cells against the devastating consequences of IFN pathway activation. The underlying mechanisms converge on the role of H3K9me2 methylation and, as such, add to the previously described role of heterochromatic DNA methylation as a safeguard against activation of an IFN response. We believe that this knowledge holds potential not only for better selection of patients with cancer for epigenetic therapies but also for the development of such.

MATERIALS AND METHODS

Experimental design

This study was performed to investigate the oncogenic effects of SUV39H1 in an AML setting and to clarify the molecular mechanism of these effects. To that end, we used two different murine in vivo AML models to test the effects of *Suv39h1* KD on tumor progression using two different shRNAs. To validate the molecular mechanism of the oncogenic effects and to understand whether the effects were comparable in humans, the human AML cell lines U937, THP-1, and Kasumi-1 were applied. RNA-seq analysis led to the hypothesis that activation of IFN pathway genes played a functional role. Western blot and ChIP-seq of H3K9 di- and trimethylation confirmed the significance of G9A/GLP destabilization for the growth phenotype. To assess the potential clinical relevance of our findings, we applied pharmacological inhibition of G9A/GLP with an inhibitor of DNA methylation.

Details on statistical methods can be found under the "Statistical analysis" section. Sample size, number of replicates, and the number of times an experiment was performed are indicated in the figure legends. No specific rules for stopping data collection were applied before initiating an experiment. All data points are shown for the included experiments. The only relevant end points were the humane end points applied in the animal experiments in concordance with Danish and European Union legislation. Randomization was applied in animal studies if the experimental animals came from different litters. Furthermore, animals from different groups were mixed between cages. Experiments were not blinded.

Plasmids

Murine shRNAs targeting *Suv39h1* were subcloned from pGIPZ into the pMLS (MSCV-LTRmir30-SV40-GFP) vector through the Xho I and Eco RI restriction sites. Human shRNAs targeting *SUV39H1* and *G9A* were cloned into the pLKO.1-puro vector (Sigma-Aldrich) via the Age I and Eco RI restriction sites, whereas *MAVS* was cloned into the pLKO.1-GFP vector with Age I and Pac I. All shRNAs can be found in table S1. WT SUV39H1 and the catalytic mutant (H324K) were overexpressed from pMIG. Briefly, human *SUV39H1* cDNA was obtained from OriGene (# sc319503 containing NM_003173) and cloned into the entry vector pCR8/GW/Topo according to the manufacturer's instructions. Subsequently, the LR Clonase reaction was performed using the entry vector and the pMIGR1/Flag-HA-GW destination vector to generate pMIGR1/Flag-HA (hemagglutinin) expression construct to express Flag-HA epitope-tagged SUV39H1 in cells of interest. For CRISPR KO, the single guide RNAs (sgRNAs) were cloned into a P2A-puro plasmid via the Bsm BI restriction site. The list of sgRNAs can be found in table S1.

Culture and treatment of cells

Lp30 murine AML cells were cultured in X-vivo 15 media (Lonza) supplemented with murine stem cell factor (SCF) (50 ng/ml), human

interleukin-6 (IL-6) (50 ng/ml), murine IL-3 (10 ng/ml) (all from PeproTech), 1% bovine serum albumin (Stem Cell Technologies), 0.1 mM β-mercaptoethanol (Sigma-Aldrich), 1% L-glutamine (Gibco), and 1% penicillin/streptomycin (pen/strep; PAA). MLL-AF9 cells were cultured in RPMI 1640 medium (Gibco, 1870-044) supplemented with 20% fetal bovine serum (FBS; Hyclone), 20% WEHI conditioned medium, SCF (20 ng/ml), IL-6 (10 ng/ml), and 1% pen/strep. MLL-AF9 cells with a stable expression of Cas9 were cultured in the same media with the further addition of blasticidin (5 μg/ml) (Gibco). c-Kit$^+$ cells were enriched using CD117 microBeads and MACS LS separation columns (Miltenyi Biotec) and grown in RPMI 1640 medium supplemented with 20% FBS, 20% WEHI, SCF (20 ng/ml), IL-6 (10 ng/ml), and 1% pen/strep. Human cell lines U937, THP-1, and Kasumi-1 were grown in RPMI 1640 medium with 10% FBS and 1% pen/strep. For the drug experiments, cells were treated with chaetocin (C9492, Sigma-Aldrich), UNC0638 (Sigma-Aldrich, U4885-5MG), and 5-AZA (Sigma-Aldrich, A2385-100mg) in the designated doses.

Flow cytometry analysis and cell sorting

Cells were sorted on FACSAriaI or FACSAriaIII (BD Biosciences) cell sorters. For GFP/YFP measurements, analysis of CD11b expression, apoptosis, and cell cycle analyses, cells were analyzed on the LSRII Cytometry System or FACSCalibur (BD Biosciences). For human cell line apoptosis analyses, transduced cells were stained with Annexin V–PE Apoptosis Detection Kit (eBioscience) according to the manufacturer's recommendations. For human cell line cell cycle analysis, transduced cells were fixed, permeabilized, and stained with propidium iodide (PI; Invitrogen). For assessment effect of nocodazole on cell cycle progression, cells were treated for 16 hours with 50 nM nocodazole (Sigma-Aldrich, SML1665), harvested, fixed, and stained with PI. For assessment of CD11b expression, transduced cells were stained with hCD11b-FITC antibody (Biosciences). All flow cytometry data were analyzed using the FlowJo 10.1 software (Tree Star, Ashland, OR, USA).

Animal studies

For competitive bone marrow transplantation assay, 100,000 transduced *shSuv39h1*-GFP–positive cells were mixed in a 1:1 ratio with *shScr*-YFP–positive cells, and transplanted by intravenous injection into sublethally irradiated [500 centigrays (cGy)] C57BL6/6J.SJL congenic recipient mice (females, 10 to 15 weeks old). Bone marrow cells were analyzed 4 weeks after transplantation.

For the survival analysis, 10,000 transduced GFP-positive Lp30 cells (shRNA KD) or GFP/YFP–double positive MLL-AF9 cells (SUV39H1 rescue) were sorted directly into phosphate-buffered saline (PBS) + 3% FBS containing a suspension of lethally irradiated (2000 cGy) bone marrow support cells (4.5×10^5 cells per mouse) and then transplanted into sublethally irradiated mice. Mice were monitored on a daily basis for disease progression and euthanized when they became moribund.

All mouse studies were conducted according to protocols approved by the Danish Animal Ethical Committee. Mice were bred and housed locally at the Department of Experimental Medicine at University of Copenhagen.

Retro- and lentivirus production and transduction

Retro- or lentiviral supernatants were generated by $CaPO_4$-mediated transfection of Phoenix E cells or human embryonic kidney 293 cells. Cell supernatants were harvested 2 days after transfection, filtered through 0.45-μm acrodisc syringe filters (Pall), and stored at −80°C.

For transduction, retroviral supernatant was added to retronectin (Takara)–coated non-tissue culture plates by centrifugation (2000*g*, 50 min, 32°C). Cells were seeded onto these virus-coated plates at a density of 1×10^6 cells/cm^2. This transduction was repeated twice, after which the cells were selected 3 days in puromycin (Sigma-Aldrich) or 6 days in blasticidin depending on the selective marker.

Western blot analysis

Whole cell lysate was prepared by lysing cell pellets in 4× laemmli buffer (Bio-Rad, 1610747) with 1:10 β-mercaptoethanol followed by dilution in high salt lysis buffer [50 mM Hepes (pH 7.5), 1 mM EDTA, and 200 mM NaCl]. The samples were resolved on NuPAGE 4 to 12% gels (Life Technologies, NP0322BOX), and proteins were transferred for 1 hour at 100 V onto polyvinylidene difluoride membranes (Millipore, IPVH00010). The membranes were incubated with primary antibodies overnight at 4°C, followed by 1 hour with secondary horseradish peroxidase antibodies (Dako, P0260 and Dako, P0217) at room temperature (RT). H3 (Abcam, ab10799) was used as loading control for histone marks and β-actin (Sigma-Aldrich, A3854-200UL) for other proteins. All antibodies used in this study can be found in table S2.

Quantification of IFN levels

Enzyme-linked immunosorbent assay (ELISA) analysis was carried out with the VeriKine Human IFN-α Multi-Subtype ELISA Kit (PBL, #41105), which can detect 14 of 15 IFN-α subtypes: IFN-αA, IFN-α2, IFN-αD, IFN-αB2, IFN-αC, IFN-αG, IFN-αH, IFN-αI, IFN-αJ1, IFN-αK, IFN-α1, IFN-α4a, IFN-α4b, and IFN-αWA. The experiment was performed on supernatant from Scrambled or *SUV39H1* KD U937 cells in biological duplicates.

RNA preparation, qRT-PCR, and RNA-seq

RNA was isolated using the Qiagen RNeasy micro kit (Qiagen, 74004), and cDNA for quantitative reverse transcription PCR (qRT-PCR) was generated using the Photoscript M-MuLV First strand cDNA synthesis kit (New England Biolabs, E6300L). A randomized primer mix was used for qRT-PCR against transposable elements, whereas an oligo-dT primer mix was used for all other applications. The $2^{-\Delta CT}$ method was used to calculate relative expression compared to *H6PD* or β-*actin* housekeeping genes. All primer sequences are provided in table S3.

RNA-seq libraries were generated from 1 μg of RNA using the TruSeq RNA Library Prep Kit v2 (Illumina, RS-122-2001). Library quantification and quality assessment were carried out on a Qubit (Life Technologies, Q32854) and on a bioanalyzer using the high-sensitivity DNA kit (Agilent, 5067 4626). The libraries were pooled in equimolar amounts and size-selected on E-Gel EX agarose, 2% (Invitrogen, G401002). DNA fragments between 200 and 500 base pairs (bp) were cut out and extracted using the MinElute Gel extraction kit (Qiagen, 28604). The size-selected libraries were diluted and sequenced according to the single-end 75-cycle HighSeq 2000 protocol.

Reads were mapped to the human genome (hg19) using STAR (*51*) with parameters (--outFilterMultimapNmax 10000; --winAnchor MultimapNmax 10000; --outSAMmultNmax 1; --alignTranscriptsPerReadNmax 15000) optimized to account for reads mapping to repeat regions in the genome. The number of reads mapping

to ensembl annotated genes (release 87, $N = 55{,}774$) was quantified using featureCounts (--countMultimapping = T; --fraction = T) (*52*, *53*). Similarly, the number of reads mapping to transposable elements (TEtranscripts annotated in human genome (hg19, $N = 992$) was quantified using featureCounts (--countMultimapping = T, --fraction = T) (*54*). Next, we selected only those genes or transposons that are expressed (at least one read) across at least two conditions, leaving us with 29,446 genes (13,693 noncoding and 15,753 protein coding) and 970 transposons. We determined genes differentially expressed between the control and treatment conditions using EdgeR (*55*). For each treatment condition (shRNA KD with Scrambled, *SUV39H1* #2, *SUV39H1* #4, *G9A* #2, *G9A* #3, and treatment with mock or G9A/GLP inhibitor), we marked a gene as differentially expressed if false discovery rate (FDR) < 0.05 and FC > 2 (up) or FC < −2 (down) across both shRNA KD and G9A/GLP inhibitor treatment. Differentially expressed genes can be found in data files S1 and S2. Data were deposited in the Gene Expression Omnibus under the accession number GSE160532.

GSEA network analysis

The GSEA analysis was carried out with the GSEA 4.0.3 application and the network created by matching the Gene Ontology (GO) terms to their corresponding GO IDs by the msigdbr v.7.1 R package. The pairwise similarity between GO IDs was calculated using goSim from the GOSemSim package using default parameters (*56*). The resulting adjacency matrix was visualized by the R igraph (*57*) package (igraph v1.2.5) using the following setup: First, a similarity score was assigned to edge weights. Then, edges with less than 20% similarity were removed. The vertex sizes were rescaled proportionally to gene set size, and the vertex pie colors at the nodes were set according to the normalized enrichment score (NES). The network was visualized using the Fruchterman-Reingold layout (*58*). Similar gene set communities were identified using the cluster_fast_greedy function from the igraph package.

Chromatin immunoprecipitation

Cells were cross-linked in 1% formaldehyde for 10 min and subsequently quenched with 0.125 M glycine for 2 min. The cells were washed twice in cold PBS and lysed in SDS buffer [100 mM NaCl, 50 mM tris-Cl (pH 8), 5 mM EDTA, 0.2% NaN_3, and 0.5% SDS] for 20 min at RT, followed by 20 min in Triton lysis buffer [100 mM NaCl, 100 mM tris-Cl (pH 8.6), 5 mM EDTA, 0.2% NaN_3, and 5% Triton X-100] on ice. The sonication was performed using a Bioruptor with 30 cycles (15 s on/30 s off). The chromatin was quantified/qualified using Qubit (Life Technologies, Q32854) and the Agilent Bioanalyzer High-Sensitivity DNA kit (Agilent, 5067-4626), and 4% *Drosophila* spike-in was added to all samples. Immunoprecipitations were done with 7 μg of chromatin from each ChIP and incubated overnight at 4°C with H3K9me3-biotinylated antibody (Diagenode, C15500003) or 2 μg of H3K9me2 antibody (Abcam, ab1220) together with protein G beads (Thermo Fisher Scientific, 10003D). The beads were washed four times in radioimmunoprecipitation assay (RIPA) buffer (140 mM NaCl, 10 mM tris-HCl, 1 mM EDTA, 1% Triton X-100, 0.1% SDS, and 0.1% sodium deoxycholate), two times in RIPA high (500 mM NaCl, 10 mM tris-HCl, 1 mM EDTA, 1% Triton X-100, 0.1% SDS, and 0.1% sodium deoxycholate), one time in LiCl buffer (250 mM LiCl, 10 mM tris-HCl, 1 mM EDTA, 0.5% NP-40, and 0.5% sodium deoxycholate), and two times in tris-EDTA buffer (10 mM tris-HCl and 1 mM EDTA) before being de–cross-linked with RNase (50 μg/ml, 30 min 37°C), SDS (0.5%), and proteinase K (1.5 mg/ml) overnight at 65°C. DNA was extracted using the minElute PCR purification kit (Qiagen, 28006). ChIP-seq libraries were generated using the NEBNext Ultra DNA Library Prep Kit with 3 ng of DNA and sequenced according to the single-end 75-cycle HighSeq 2000 protocol.

H3K9me2 ChIP-seq reads were mapped to a combined genome assembly of human (hg19) and *Drosophila melanogaster* (dm6) using bowtie2 (*59*), and reads mapping to multiple regions in the human genome were kept to account for expression of repeat regions in the genome. Total reads mapping to the *Drosophila* genome were used to determine the scaling factor, which was later used for spike-in normalization. PCR duplicates were identified using samtools markdup (*60*) and collapsed to one read. H3K9me2 enrichment at gene bodies (ensembl annotated, hg19 release 87, $N = 55{,}774$) and transposons (TEtranscripts annotated, hg19, $N = 992$) was computed using featureCounts (--countMultimapping = T, --fraction = T) and subsequently spike-in normalized (*52*–*54*).

H3K9me3 ChIP-seq reads were mapped to the hg19 genome assembly using bowtie2 (*59*), and reads mapping to multiple regions in the human genome were kept to account for expression of repeat regions in the genome. PCR duplicates were identified using samtools markdup (*60*) and were collapsed to one read. H3K9me3 enrichment at gene bodies and transposons was computed as done for the aforementioned H3K9me2 enrichment analysis.

For both H3K9me2 and H3K9me3, we selected genes or transposons that are expressed (at least one read) across at least two conditions, leaving us with 39,017 H3K9me2-enriched regions (20,047 noncoding, 17,978 protein coding, and 992 transposons) and 39,288 H3K9me3-enriched regions (20,230 noncoding, 18,066 protein coding, and 992 transposons). Next, we identified regions differentially enriched for H3K9me2 or H3K9me3 between two replicates each of scrambled and treatment conditions using EdgeR (*55*). For each treatment condition, we marked regions as differentially enriched if FDR < 0.05 and FC > 2 (up) or FC < −2 (down) across both treatment conditions. Data were deposited in the Gene Expression Omnibus under the accession number GSE160532.

Drug testing

U937 cells were preincubated in mock or different 5-AZA (0 to 1 μg/ml) concentrations for 3 days, with media changes every day. Subsequently, the preincubated cells were grown in mock or UNC0638 (0 to 7 μM) for an additional 3 days and the cell number was determined using NucleoCounter solution 13 (910-3013, Chemometric). The ZIP score, a synergy score model, was calculated using the SynergyFinder (*61*). For assays using fixed concentrations/expression levels of the individual effectors, the level of synergy on gene expression was calculated using the coefficient of drug interaction (CDI), which is calculated as AB/A*B, where A, B and AB depict either of the two agents and the two agents in combination, respectively. In the case of target gene induction, CDI < 1, CDI = 1, and CDI > 1 indicate an antagonistic, an additive, and a synergistic effect of the two agents, respectively.

For drug response assays in primary bone marrow material, we selected three AML samples and one nonmalignant sample of Ficoll isolated mononuclear cells. Samples were thawed in RPMI (Thermo Fisher Scientific) + 20% FBS (Thermo Fisher Scientific) + 1% pen/strep (Gibco) + TurboNuclease (50 U/ml) (Abnova), counted, and resuspended in StemSpanSFEM II (StemCell) + pen/strep (100 U/ml)

at 1×10^6 cells/ml. The cells were allowed to rest overnight at 37°C (5% CO_2).

UNC0638 dissolved in dimethyl sulfoxide (DMSO) (Merck), or DMSO alone, was added to a 384-well v-bottom assay plate (Greiner) at the desired concentrations using an Echo550 (Labcyte). In all wells, the final concentration of DMSO is 0.1%. The rested cells were then spun and resuspended in assay media [StemSpanSFEM II + 1% pen/strep + TPO (Thrombopoietin) + SCF (both from PeproTech) + StemRegenin1 (MedChemExpress)] and added to the wells at a density of 15,000 cells per well. The assay plate was incubated for 72 hours at 37°C (5% CO_2). The live/dead marker Draq7 (BioLegend) was transferred to the assay plate using an Echo550, incubated for 1 hour at RT before being run on the iQue FACS machine (Sartorius).

Whole-genome bisulfite sequencing

Genomic DNA was fragmented to a size of 450 bp in a Covaris M220 Focused-Ultrasonicater and size distribution was measured with the Bioanalyzer High-Sensitivity DNA kit (Agilent, 5067-4626).

The EZ DNA Methylation-Gold Kit (Zymo Research, D5005) was used to convert unmethylated cytosine residues of the fragmented genomic DNA (500 ng) into uracil. The concentration and quality of the converted DNA were measured using the Bioanalyzer RNA 6000 Pico Kit (Agilent, 5067-1513). Subsequently, the Pico Methyl-Seq Library Prep Kit (Zymo Research, D5455) was used to generate the libraries and sequenced using an S2 flow cells on the NovaSeq 6000 sequencing system. Paired-end (150 bp) reads were randomly subsampled to 100 million reads using the seqtk package (-s100 parameter) (https://github.com/lh3/seqtk) and aligned to human genome (hg19 assembly) using bwa-meth (v0.2.2, default parameters) (https://arxiv.org/abs/1401.1129). PCR duplicate reads were marked using the markdup function of the sambamba package (v0.6.8) (https://lomereiter.github.io/sambamba/). DNA methylation levels were analyzed using MethylDackel (v0.3.0). First, we used the mbias function of MethylDackel to compute the 5′ and 3′ end position of reads that show disproportionate levels of methylated CpGs. These positions were excluded in the downstream analysis using the extract function of MethyDackel (--OT and --OB parameters). The bedGraph files from MethyDackel were used to compute the DNA methylation fraction at CpG dinucleotides using the methrix package (v1.4.7; pipeline = "MethyDackel", stranded = F, zero_based = F, collapse_strands = F parameters) (https://pubmed.ncbi.nlm.nih.gov/33346800/).

Analysis of patient data

The data from AML patients were obtained from Tyner *et al.* (*39*) and sorted via cBioPortal (www.cbioportal.org) based on "current treatment" for each AML patient. All patients, or patients treated with hypomethylation agent in combination with low-dose cytarabine, were organized into groups with the 40% highest and 40% lowest expression of *SUV39H1*, *G9A*, or *GLP*. Overall survival or IFN expression was addressed in the high- and low-*SUV39H1* groups.

Statistical analysis

Sample sizes were not predetermined but are indicated in relevant figures. No blinding of experimental groups was performed. The number of times an experiment was performed is indicated in the figure legends. All statistical analyses were performed using Prism version 7.0 software (GraphPad Software Inc.). Comparisons between groups were performed by a two-tailed Student's *t* test, while a log-rank test was used to assess significant differences between survival curves. To determine the significant levels of ChIP-seq tracks on specific genes, we used a one-tailed Wilcoxon test. Sample sizes chosen are indicated in the individual figure legends. $P < 0.05$ was considered to be significant. The results were represented as means ± SD. *$P < 0.05$; **$P < 0.01$; ***$P < 0.001$; ****$P < 0.0001$. SDs are indicated on all figure panels.

SUPPLEMENTARY MATERIALS

Supplementary material for this article is available at https://science.org/doi/10.1126/sciadv.abf8627

View/request a protocol for this paper from *Bio-protocol*.

REFERENCES AND NOTES

1. A. Burnett, M. Wetzler, B. Lowenberg, Therapeutic advances in acute myeloid leukemia. *J. Clin. Oncol.* **29**, 487–494 (2011).
2. D. Hanahan, Hallmarks of cancer: The next generation. *Cell* **144**, 646–674 (2011).
3. J. Luo, N. L. Solimini, S. J. Elledge, Principles of cancer therapy: Oncogene and non-oncogene addiction. *Cell* **136**, 823–837 (2009).
4. A. H. Shih, O. Abdel-Wahab, J. P. Patel, R. L. Levine, The role of mutations in epigenetic regulators in myeloid malignancies. *Nat. Rev. Cancer* **12**, 599–612 (2012).
5. O. Abdel-Wahab, R. L. Levine, Mutations in epigenetic modifiers in the pathogenesis and therapy of acute myeloid leukemia. *Blood* **121**, 3563–3572 (2013).
6. S. Rea, F. Eisenhaber, D. O'Carroll, B. D. Strahl, Z. W. Sun, M. Schmid, S. Opravil, K. Mechtler, C. P. Ponting, C. D. Allis, T. Jenuwein, Regulation of chromatin structure by site-specific histone H3 methyltransferases. *Nature* **406**, 593–599 (2000).
7. D. O'Carroll, H. Scherthan, A. H. Peters, S. Opravil, A. R. Haynes, G. Laible, S. Rea, M. Schmid, A. Lebersorger, M. Jerratsch, L. Sattler, M. G. Mattei, P. Denny, S. D. Brown, D. Schweizer, T. Jenuwein, Isolation and characterization of Suv39h2, a second histone H3 methyltransferase gene that displays testis-specific expression. *Mol. Cell. Biol.* **20**, 9423–9433 (2000).
8. M. Lachner, D. O'Carroll, S. Rea, K. Mechtler, T. Jenuwein, Methylation of histone H3 lysine 9 creates a binding site for HP1 proteins. *Nature* **410**, 116–120 (2001).
9. A. H. Peters, D. O'Carroll, H. Scherthan, K. Mechtler, S. Sauer, C. Schöfer, K. Weipoltshammer, M. Pagani, M. Lachner, A. Kohlmaier, S. Opravil, M. Doyle, M. Sibilia, T. Jenuwein, Loss of the Suv39h histone methyltransferases impairs mammalian heterochromatin and genome stability. *Cell* **107**, 323–337 (2001).
10. M. García-Cao, R. O'Sullivan, A. H. F. M. Peters, T. Jenuwein, M. A. Blasco, Epigenetic regulation of telomere length in mammalian cells by the Suv39h1 and Suv39h2 histone methyltransferases. *Nat. Genet.* **36**, 94–99 (2004).
11. D. Spensberger, R. Delwel, A novel interaction between the proto-oncogene Evi1 and histone methyltransferases, SUV39H1 and G9a. *FEBS Lett.* **582**, 2761–2767 (2008).
12. F. Cattaneo, G. Nucifora, EVI1 recruits the histone methyltransferase SUV39H1 for transcription repression. *J. Cell. Biochem.* **105**, 344–352 (2008).
13. S. Goyama, E. Nitta, T. Yoshino, S. Kako, N. Watanabe-Okochi, M. Shimabe, Y. Imai, K. Takahashi, M. Kurokawa, EVI-1 interacts with histone methyltransferases SUV39H1 and G9a for transcriptional repression and bone marrow immortalization. *Leukemia* **24**, 81–88 (2010).
14. S. Chakraborty, K. K. Sinha, V. Senyuk, G. Nucifora, SUV39H1 interacts with AML1 and abrogates AML1 transactivity. AML1 is methylated in vivo. *Oncogene* **22**, 5229–5237 (2003).
15. R. Carbone, O. A. Botrugno, S. Ronzoni, A. Insinga, L. di Croce, P. G. Pelicci, S. Minucci, Recruitment of the histone methyltransferase SUV39H1 and its role in the oncogenic properties of the leukemia-associated PML-retinoic acid receptor fusion protein. *Mol. Cell. Biol.* **26**, 1288–1296 (2006).
16. A. Lakshmikuttyamma, S. A. Scott, J. F. DeCoteau, C. R. Geyer, Reexpression of epigenetically silenced AML tumor suppressor genes by SUV39H1 inhibition. *Oncogene* **29**, 576–588 (2010).
17. L. Fritsch, P. Robin, J. R. R. Mathieu, M. Souidi, H. Hinaux, C. Rougeulle, A. Harel-Bellan, M. Ameyar-Zazoua, S. Ait-Si-Ali, A subset of the histone H3 lysine 9 methyltransferases Suv39h1, G9a, GLP, and SETDB1 participate in a multimeric complex. *Mol. Cell* **37**, 46–56 (2010).
18. D. Roulois, H. Loo Yau, R. Singhania, Y. Wang, A. Danesh, S. Y. Shen, H. Han, G. Liang, P. A. Jones, T. J. Pugh, C. O'Brien, D. D. de Carvalho, DNA-demethylating agents target colorectal cancer cells by inducing viral mimicry by endogenous transcripts. *Cell* **162**, 961–973 (2015).

19. K. B. Chiappinelli, P. L. Strissel, A. Desrichard, H. Li, C. Henke, B. Akman, A. Hein, N. S. Rote, L. M. Cope, A. Snyder, V. Makarov, S. Buhu, D. J. Slamon, J. D. Wolchok, D. M. Pardoll, M. W. Beckmann, C. A. Zahnow, T. Merghoub, T. A. Chan, S. B. Baylin, R. Strick, Inhibiting DNA methylation causes an interferon response in cancer via dsRNA including endogenous retroviruses. *Cell* **162**, 974–986 (2015).
20. A. Bulut-Karslioglu, I. A. de la Rosa-Velázquez, F. Ramirez, M. Barenboim, M. Onishi-Seebacher, J. Arand, C. Galán, G. E. Winter, B. Engist, B. Gerle, R. J. O'Sullivan, J. H. A. Martens, J. Walter, T. Manke, M. Lachner, T. Jenuwein, Suv39h-dependent H3K9me3 marks intact retrotransposons and silences LINE elements in mouse embryonic stem cells. *Mol. Cell* **55**, 277–290 (2014).
21. M. Ehrlich, DNA methylation in cancer: Too much, but also too little. *Oncogene* **21**, 5400–5413 (2002).
22. M. Kulis, M. Esteller, DNA methylation and cancer. *Adv. Genet.* **70**, 27–56 (2010).
23. H. Chaib, A. Nebbioso, T. Prebet, R. Castellano, S. Garbit, A. Restouin, N. Vey, L. Altucci, Y. Collette, Anti-leukemia activity of chaetocin via death receptor-dependent apoptosis and dual modulation of the histone methyl-transferase SUV39H1. *Leukemia* **26**, 662–674 (2012).
24. Y. S. Lai, J. Y. Chen, H. J. Tsai, T. Y. Chen, W. C. Hung, The SUV39H1 inhibitor chaetocin induces differentiation and shows synergistic cytotoxicity with other epigenetic drugs in acute myeloid leukemia cells. *Blood Cancer J.* **5**, e313 (2015).
25. D. Greiner, T. Bonaldi, R. Eskeland, E. Roemer, A. Imhof, Identification of a specific inhibitor of the histone methyltransferase SU(VAR)3-9. *Nat. Chem. Biol.* **1**, 143–145 (2005).
26. Y. Ge, M. B. Schuster, S. Pundhir, N. Rapin, F. O. Bagger, N. Sidiropoulos, N. Hashem, B. T. Porse, The splicing factor RBM25 controls MYC activity in acute myeloid leukemia. *Nat. Commun.* **10**, 172 (2019).
27. J. S. Jakobsen, L. G. Laursen, M. B. Schuster, S. Pundhir, E. Schoof, Y. Ge, T. d'Altri, K. Vitting-Seerup, N. Rapin, C. Gentil, J. Jendholm, K. Theilgaard-Mönch, K. Reckzeh, L. Bullinger, K. Döhner, P. Hokland, J. Fitzgibbon, B. T. Porse, Mutant CEBPA directly drives the expression of the targetable tumor-promoting factor CD73 in AML. *Sci. Adv.* **5**, eaaw4304 (2019).
28. T. C. Somervaille, M. L. Cleary, Identification and characterization of leukemia stem cells in murine MLL-AF9 acute myeloid leukemia. *Cancer Cell* **10**, 257–268 (2006).
29. A. P. West, G. S. Shadel, S. Ghosh, Mitochondria in innate immune responses. *Nat. Rev. Immunol.* **11**, 389–402 (2011).
30. V. Hornung, R. Hartmann, A. Ablasser, K. P. Hopfner, OAS proteins and cGAS: Unifying concepts in sensing and responding to cytosolic nucleic acids. *Nat. Rev. Immunol.* **14**, 521–528 (2014).
31. T. C. Fang, U. Schaefer, I. Mecklenbrauker, A. Stienen, S. Dewell, M. S. Chen, I. Rioja, V. Parravicini, R. K. Prinjha, R. Chandwani, M. R. MacDonald, K. Lee, C. M. Rice, A. Tarakhovsky, Histone H3 lysine 9 di-methylation as an epigenetic signature of the interferon response. *J. Exp. Med.* **209**, 661–669 (2012).
32. B. S. Parker, J. Rautela, P. J. Hertzog, Antitumour actions of interferons: Implications for cancer therapy. *Nat. Rev. Cancer* **16**, 131–144 (2016).
33. M. Vedadi, D. Barsyte-Lovejoy, F. Liu, S. Rival-Gervier, A. Allali-Hassani, V. Labrie, T. J. Wigle, P. A. DiMaggio, G. A. Wasney, A. Siarheyeva, A. Dong, W. Tempel, S. C. Wang, X. Chen, I. Chau, T. J. Mangano, X. P. Huang, C. D. Simpson, S. G. Pattenden, J. L. Norris, D. B. Kireev, A. Tripathy, A. Edwards, B. L. Roth, W. P. Janzen, B. A. Garcia, A. Petronis, J. Ellis, P. J. Brown, S. V. Frye, C. H. Arrowsmith, J. Jin, A chemical probe selectively inhibits G9a and GLP methyltransferase activity in cells. *Nat. Chem. Biol.* **7**, 566–574 (2011).
34. K. C. Kim, L. Geng, S. Huang, Inactivation of a histone methyltransferase by mutations in human cancers. *Cancer Res.* **63**, 7619–7623 (2003).
35. G. H. Eom, K. Kim, S. M. Kim, H. J. Kee, J. Y. Kim, H. M. Jin, J. R. Kim, J. H. Kim, N. Choe, K. B. Kim, J. Lee, H. Kook, N. Kim, S. B. Seo, Histone methyltransferase PRDM8 regulates mouse testis steroidogenesis. *Biochem. Biophys. Res. Commun.* **388**, 131–136 (2009).
36. F. Fuks, P. J. Hurd, R. Deplus, T. Kouzarides, The DNA methyltransferases associate with HP1 and the SUV39H1 histone methyltransferase. *Nucleic Acids Res.* **31**, 2305–2312 (2003).
37. S. C. Navada, J. Steinmann, M. Lübbert, L. R. Silverman, Clinical development of demethylating agents in hematology. *J. Clin. Invest.* **124**, 40–46 (2014).
38. B. Yadav, K. Wennerberg, T. Aittokallio, J. Tang, Searching for drug synergy in complex dose–response landscapes using an interaction potency model. *Comput. Struct. Biotechnol. J.* **13**, 504–513 (2015).
39. J. W. Tyner, C. E. Tognon, D. Bottomly, B. Wilmot, S. E. Kurtz, S. L. Savage, N. Long, A. R. Schultz, E. Traer, M. Abel, A. Agarwal, A. Blucher, U. Borate, J. Bryant, R. Burke, A. Carlos, R. Carpenter, J. Carroll, B. H. Chang, C. Coblentz, A. d'Almeida, R. Cook, A. Danilov, K. H. T. Dao, M. Degnin, D. Devine, J. Dibb, D. K. Edwards V, C. A. Eide, I. English, J. Glover, R. Henson, H. Ho, A. Jemal, K. Johnson, R. Johnson, B. Junio, A. Kaempf, J. Leonard, C. Lin, S. Q. Liu, P. Lo, M. M. Loriaux, S. Luty, T. Macey, J. MacManiman, J. Martinez, M. Mori, D. Nelson, C. Nichols, J. Peters, J. Ramsdill, A. Rofelty, R. Schuff, R. Searles, E. Segerdell, R. L. Smith, S. E. Spurgeon, T. Sweeney, A. Thapa, C. Visser, J. Wagner, K. Watanabe-Smith, K. Werth, J. Wolf, L. White, A. Yates, H. Zhang, C. R. Cogle, R. H. Collins, D. C. Connolly, M. W. Deininger, L. Drusbosky, C. S. Hourigan, C. T. Jordan, P. Kropf, T. L. Lin, M. E. Martinez, B. C. Medeiros, R. R. Pallapati, D. A. Pollyea, R. T. Swords, J. M. Watts, S. J. Weir, D. L. Wiest, R. M. Winters, S. K. McWeeney, B. J. Druker, Functional genomic landscape of acute myeloid leukaemia. *Nature* **562**, 526–531 (2018).
40. B. Lehnertz, C. Pabst, L. Su, M. Miller, F. Liu, L. Yi, R. Zhang, J. Krosl, E. Yung, J. Kirschner, P. Rosten, T. M. Underhill, J. Jin, J. Hébert, G. Sauvageau, R. K. Humphries, F. M. Rossi, The methyltransferase G9a regulates HoxA9-dependent transcription in AML. *Genes Dev.* **28**, 317–527 (2014).
41. H. J. Son, J. Y. Kim, Y. Hahn, S. B. Seo, Negative regulation of JAK2 by H3K9 methyltransferase G9a in leukemia. *Mol. Cell. Biol.* **32**, 3681–3694 (2012).
42. J. Y. Kim, K. B. Kim, G. H. Eom, N. Choe, H. J. Kee, H. J. Son, S. T. Oh, D. W. Kim, J. H. Pak, H. J. Baek, H. Kook, Y. Hahn, H. Kook, D. Chakravarti, S. B. Seo, KDM3B is the H3K9 demethylase involved in transcriptional activation of lmo2 in leukemia. *Mol. Cell. Biol.* **32**, 2917–2933 (2012).
43. E. S. José-Enériz, X. Agirre, O. Rabal, A. Vilas-Zornoza, J. A. Sanchez-Arias, E. Miranda, A. Ugarte, S. Roa, B. Paiva, A. E.-H. de Mendoza, R. M. Alvarez, N. Casares, V. Segura, J. I. Martín-Subero, F.-X. Ogi, P. Soule, C. M. Santiveri, R. Campos-Olivas, G. Castellano, M. G. F. de Barrena, J. R. Rodriguez-Madoz, M. J. García-Barchino, J. J. Lasarte, M. A. Avila, J. A. Martinez-Climent, J. Oyarzabal, F. Prosper, Discovery of first-in-class reversible dual small molecule inhibitors against G9a and DNMTs in hematological malignancies. *Nat. Commun.* **8**, 15424 (2017).
44. A. C. Salzberg, A. Harris-Becker, E. Y. Popova, N. Keasey, T. P. Loughran, D. F. Claxton, S. A. Grigoryev, Genome-wide mapping of histone H3K9me2 in acute myeloid leukemia reveals large chromosomal domains associated with massive gene silencing and sites of genome instability. *PLOS ONE* **12**, e0173723 (2017).
45. S. Sharma, D. S. Gerke, H. F. Han, S. Jeong, M. R. Stallcup, P. A. Jones, G. Liang, Lysine methyltransferase G9a is not required for DNMT3A/3B anchoring to methylated nucleosomes and maintenance of DNA methylation in somatic cells. *Epigenetics Chromatin* **5**, 3 (2012).
46. M. Liu, S. L. Thomas, A. DeWitt, W. Zhou, Z. B. Madaj, H. Ohtani, S. B. Baylin, G. Liang, P. A. Jones, Dual Inhibition of DNA and histone methyltransferases increases viral mimicry in ovarian cancer cells. *Cancer Res.* **78**, 5754–5766 (2018).
47. C. Segovia, E. San José-Enériz, E. Munera-Maravilla, M. Martínez-Fernández, L. Garate, E. Miranda, A. Vilas-Zornoza, I. Lodewijk, C. Rubio, C. Segrelles, L. V. Valcárcel, O. Rabal, N. Casares, A. Bernardini, C. Suarez-Cabrera, F. F. López-Calderón, P. Fortes, J. A. Casado, M. Dueñas, F. Villacampa, J. J. Lasarte, F. Guerrero-Ramos, G. de Velasco, J. Oyarzabal, D. Castellano, X. Agirre, F. Prósper, J. M. Paramio, Inhibition of a G9a/DNMT network triggers immune-mediated bladder cancer regression. *Nat. Med.* **25**, 1073–1081 (2019).
48. U. Y. Choi, J. S. Kang, Y. S. Hwang, Y. J. Kim, Oligoadenylate synthase-like (OASL) proteins: Dual functions and associations with diseases. *Exp. Mol. Med.* **47**, e144 (2015).
49. K. Malathi, B. Dong, M. Gale Jr., R. H. Silverman, Small self-RNA generated by RNase L amplifies antiviral innate immunity. *Nature* **448**, 816–819 (2007).
50. S. Kudithipudi, M. K. Schuhmacher, A. F. Kebede, A. Jeltsch, The SUV39H1 protein lysine methyltransferase methylates chromatin proteins involved in heterochromatin formation and VDJ recombination. *ACS Chem. Biol.* **4**, 958–968 (2017).
51. A. Dobin, C. A. Davis, F. Schlesinger, J. Drenkow, C. Zaleski, S. Jha, P. Batut, M. Chaisson, T. R. Gingeras, STAR: Ultrafast universal RNA-seq aligner. *Bioinformatics* **29**, 15–21 (2013).
52. Y. Liao, G. K. Smyth, W. Shi, featureCounts: An efficient general purpose program for assigning sequence reads to genomic features. *Bioinformatics* **30**, 923–930 (2014).
53. A. D. Yates, P. Achuthan, W. Akanni, J. Allen, J. Allen, J. Alvarez-Jarreta, M. R. Amode, I. M. Armean, A. G. Azov, R. Bennett, J. Bhai, K. Billis, S. Boddu, J. C. Marugán, C. Cummins, C. Davidson, K. Dodiya, R. Fatima, A. Gall, C. G. Giron, L. Gil, T. Grego, L. Haggerty, E. Haskell, T. Hourlier, O. G. Izuogu, S. H. Janacek, T. Juettemann, M. Kay, I. Lavidas, T. le, D. Lemos, J. G. Martinez, T. Maurel, M. McDowall, A. McMahon, S. Mohanan, B. Moore, M. Nuhn, D. N. Oheh, A. Parker, A. Parton, M. Patricio, M. P. Sakthivel, A. I. Abdul Salam, B. M. Schmitt, H. Schuilenburg, D. Sheppard, M. Sycheva, M. Szuba, K. Taylor, A. Thormann, G. Threadgold, A. Vullo, B. Walts, A. Winterbottom, A. Zadissa, M. Chakiachvili, B. Flint, A. Frankish, S. E. Hunt, G. Ilsley, M. Kostadima, N. Langridge, J. E. Loveland, F. J. Martin, J. Morales, J. M. Mudge, M. Muffato, E. Perry, M. Ruffier, S. J. Trevanion, F. Cunningham, K. L. Howe, D. R. Zerbino, P. Flicek, Ensembl 2020. *Nucleic Acids Res.* **48** (D1), D682–D688 (2020).
54. Y. Jin, O. H. Tam, E. Paniagua, M. Hammell, TEtranscripts: A package for including transposable elements in differential expression analysis of RNA-seq datasets. *Bioinformatics* **31**, 3593–3599 (2015).
55. Y. Chen, D. Mccarthy, M. Robinson, G. K. Smyth, edgeR: Differential expression analysis of digital gene expression data. User's Guide (2014).
56. G. Yu, F. Li, Y. Qin, X. Bo, Y. Wu, S. Wang, GOSemSim: An R package for measuring semantic similarity among GO terms and gene products. *Bioinformatics* **26**, 976–978 (2010).
57. G. N. T. Csardi, The igraph software package for complex network research. InterJournal, Complex Systems 1695 (2005).
58. J. Fruchterman, M. Reingold, Graph drawing by force-directed placement. Software: Practice and experience. *Sci. Res.* **21**, 1129–1164 (1991).

59. B. Langmead, S. L. Salzberg, Fast gapped-read alignment with Bowtie 2. *Nat. Methods* **9**, 357–359 (2012).
60. H. Li, B. Handsaker, A. Wysoker, T. Fennell, J. Ruan, N. Homer, G. Marth, G. Abecasis, R. Durbin; 1000 Genome Project Data Processing Subgroup, The sequence alignment/map format and SAMtools. *Bioinformatics* **25**, 2078–2079 (2009).
61. A. Ianevski, A. K. Giri, T. Aittokallio, SynergyFinder 2.0: Visual analytics of multi-drug combination synergies. *Nucleic Acids Res.* **48** (W1), W488–W493 (2020).
62. I. Rusinova, S. Forster, S. Yu, A. Kannan, M. Masse, H. Cumming, R. Chapman, P. J. Hertzog, Interferome v2.0: An updated database of annotated interferon-regulated genes. *Nucleic Acids Res.* **41** (Database issue), D1040–D1046 (2013).

Acknowledgments: We thank members of the Porse Lab for discussions. **Funding:** This study was supported by grants from the Karen Elise Jensen Foundation, the Becket Foundation, the Danish Association for Cancer Research, the Novo Nordisk Foundation (NNF6347), the Copenhagen University Hospital, the Capital Region of Copenhagen, and the Danish Cancer Society (R90-A5791), and by a center grant from the Novo Nordisk Foundation (Novo Nordisk Foundation Center for Stem Cell Biology, DanStem; grant number NNF17CC0027852). Last, this work is part of the Danish Research Center for Precision Medicine in Blood Cancers funded by the Danish Cancer Society (R223-A13071) and Greater Copenhagen Health Science Partners. **Author contributions:** Y.G., A.M.H., M.B.S., S.G., F.A., and D.P. performed experiments. Y.G., A.M.H., M.B.S., S.P., J.S.J., A.K., F.O.B., K.H., S.G., F.A., and B.T.P. analyzed data. Y.G., A.M.H., M.B.S., J.S.J., S.G., F.A., and B.T.P. designed experiments. A.M.H., M.B.S., and B.T.P. drafted the manuscript. All authors have proofread and approved the final version of the manuscript. **Competing interests:** The authors declare that they have no competing interests. **Data and materials availability:** All data needed to evaluate the conclusions in the paper are present in the paper, the Supplementary Materials, or the Gene Expression Omnibus under the accession number GSE160532.

Submitted 24 November 2020
Accepted 26 January 2022
Published 18 March 2022
10.1126/sciadv.abf8627